buildings

MDPI

Article

Progressive Collapse Resistance of RC Beam–Slab Substructures Made with Rubberized Concrete

Ibrahim M. H. Alshaikh [1,*], Aref A. Abadel [2,*], Khaled Sennah [3], Moncef L. Nehdi [4,*], Rabin Tuladhar [5] and Mohammed Alamri [2]

[1] School of Civil Engineering, Engineering Campus, University Sains Malaysia, Penang 14300, Malaysia
[2] Department of Civil Engineering, College of Engineering, King Saud University, Riyadh 11421, Saudi Arabia
[3] Department of Civil Engineering, Toronto Metropolitan University, Toronto, ON 66777, Canada
[4] Department of Civil Engineering, McMaster University, Hamilton, ON L8S 4L8, Canada
[5] College of Science & Engineering, James Cook University, Townsville, QLD 4811, Australia
* Correspondence: ibrahimalshaikh86@gmail.com (I.M.H.A.); aabadel@ksu.edu.sa (A.A.A.); nehdim@mcmaster.ca (M.L.N.)

Abstract: Abnormal loads can produce localized damage that can eventually cause progressive collapse of the whole reinforced concrete (RC) structure. This might have devastating financial repercussions and cause numerous severe casualties. Numerical simulation, using the finite element method (FEM), of the consequences of abnormal loads on buildings is thus required to avoid the significant expenses associated with testing full-scale buildings and to save time. In this paper, FEM simulations, using ABAQUS software, were employed to investigate the progressive collapse resistance of the full-scale three-dimensional (3D) beam–slab substructures, considering two concrete mixes, namely: normal concrete (NC) and rubberized concrete (RuC) which was made by incorporating crumb rubber at 20% by volume replacement for sand. The FEM accuracy and dependability were validated using available experimental test results. Concrete and steel material non-linearity were considered in the FE modelling. The numerical study is extended to include eight new models with various specifics (a set of parameters) for further understanding of progressive collapse. Results showed that slabs contribute more than a third of the load resistance, which also significantly improves the building's progressive collapse resistance. Moreover, the performance of the RuC specimens was excellent in the catenary stage, which develops additional resilience to significant deformation to prevent or even mitigate progressive collapse.

Keywords: progressive collapse; beam–slab structures; rubberized concrete; catenary action; tensile membrane action; numerical simulation; finite element modelling; ABAQUS software

Citation: Alshaikh, I.M.H.; Abadel, A.A.; Sennah, K.; Nehdi, M.L.; Tuladhar, R.; Alamri, M. Progressive Collapse Resistance of RC Beam–Slab Substructures Made with Rubberized Concrete. *Buildings* **2022**, *12*, 1724. https://doi.org/10.3390/buildings12101724

Academic Editor: Oldrich Sucharda

Received: 16 September 2022
Accepted: 13 October 2022
Published: 18 October 2022

1. Introduction

Progressive collapse of a reinforced concrete (RC) structure is a disproportionate failure mode in which initial local damage caused by accidental loading conditions gradually leads to a much larger part collapse or even a complete structural collapse [1]. Numerous progressive collapse events over the past few decades [2–4] resulting from terrorist attacks or abnormal loads have resulted in significant losses of life and property. The unexpected partial failure of a building in Miami, USA, which happened recently in 2021 [5], serves as a reminder to designers, researchers, and professionals of the significance of RC structural integrity and robustness in particular [6]. Various building standards [1,7,8] and design guidelines [9–11] have been published in an effort to stop these collapse accidents. Some design approaches to prevent progressive collapses, such as the tie force (TF) method and alternate load path (ALP) method, were introduced in these guidelines. One significant strategy for preventing progressive collapse is to use ductile materials when building structures. In addition, researchers have created novel techniques for improving progressive collapse resistance, including improvements in reinforcement detailing [12–14], using

carbon fiber reinforced polymer (CFRP) [15–17], and partial de-bonding of reinforcing rebars [18]. These implemented strategies showed improved progressive collapse resistance. The most commonly used building material worldwide is concrete. Concrete has a colossal environmental footprint, particularly in terms of CO_2 emissions. Therefore, it is necessary to incorporate sustainability criteria into performance-based design and assessment, and this has become a top research priority globally in recent years [19,20]. The capacity of RC members to sustain sizable deformations without substantial crashing before ultimate collapse is known as ductility. Therefore, a ductile member has the potential to absorb energy without experiencing a catastrophic failure, which improves the progressive collapse resistance or even mitigates it. Many researchers have examined the viability of using waste tires to produce concrete in recent decades. That extensive effort attempts to address a significant environmental problem brought on by the accumulation of thousands of waste tires around the world by making it simple to reuse enormous volumes of waste materials as replacement aggregate in asphalt and concrete [21,22]. Because rubber compounds are difficult to biodegrade, disposing waste tires has become a significant environmental problem on a global scale [23,24]. The annual accumulation of tens of thousands of waste tires makes this issue worse [25]. Tire disposal practices that are typically inappropriate include burning tires or piling them up in landfills, which lead to significant environmental issues. Rubber use was found to have a significant positive impact on the dynamic characteristics of concrete, impact resistance, ductility, and strain capacity [21,26] Waste tires were used as crumb rubber with an acceptable replacement level for sand in concrete mixtures, which enhanced deformability and ductility [26–32]. It is possible that this rubberized concrete (RuC) will increase resistance to progressive collapse. The majority of experimental research found in the literature has concentrated on RC beam–column subassemblies, the specimens are made up of two exterior-column connected by a two-span beam and an interior-column stub at the middle joint, which represents the failed or removed column [12,16,18,33–37]. Notably, most recent research has largely neglected the role that floor slabs play in resisting progressive collapse [38]. However, RC slabs are crucial for redistributing failed column loads following initial local failures in RC structures. Under various stress levels, RC slabs offer additional resistance by compressive membrane action (CMA) or tensile membrane action (TMA). Kang et al. [39] analytically studied the development of CMA and TMA in one-way RC beam–slab sub-structures. After the validation of the models, various parameters were investigated. Their results indicated that the width and thickness of the RC slab affect the deformation capacity of one-way beam–slab sub-structures, while the cross-sectional area of longitudinal reinforcing rebars in the slab affects the TMA capacity. Qian and Li [15,40–42] carried out a sets of progressive collapse tests on beam–slab subassemblies under scenarios of removing the corner and middle columns to investigate the slab effects. According to their test results, the probability of progressive collapse can be considerably decreased by taking the slab contribution into account. Because of its benefits, including cost savings, time savings, and the ability to test full-scale specimens numerically, the finite element method (FEM) has been widely used nowadays. The FEM simulation is superior in the progressive collapse field since the entire building can be modelled. The finite element (FE) models, which employ commercial programs, can more accurately and reliably simulate the performance of RC structures under impact and assist in investigating different design variables (e.g., [43,44]). Despite the rise in the quantity of scientific articles published, the majority of experimental and numerical studies undertaken focused on the effect of reinforcing rebars by increasing flexural reinforcement ratios, adding new rebar layers or changing the seismic reinforcing detailing of RC beams to prevent progressive collapse. Additionally, the evaluation of the progressive collapse of RC structures made with special or rubberized concrete is an important construction field that needs to be investigated, according to reviews previously carried out by Alshaikh et al. [45] and Kiakojouri et al. [46] and as discussed in various studies [47–49]. However, there is a paucity of information on the addition of waste tires (i.e., crumb rubber) in concrete mixtures to enhance the progressive collapse resistance, with the exception of a few previous stud-

ies (i.e., [47,49,50]). Additionally, there is a lack of information on large-scale testing to look into the viability of using RuC in structural applications especially progressive collapse tests. Additionally, studies on rubberized concrete resistance to progressive collapse of the three-dimensional (3D) beam–slab structures are as yet unavailable. Accordingly, the main goal of this study is to offer useful insights into how the addition of crumb rubber affects the overall performance of RC beam–slab structures in terms of resistance to progressive collapse, which can yield economic and environmental benefits at the same time. In this paper, numerical simulations were employed to investigate the progressive collapse resistance of full-scale 3D beam–slab structures, considering two concrete mixtures (i.e., normal and rubberized concrete) by utilizing the program ABAQUS-Explicit. The accuracy and dependability of the FE models were improved and validated by comparing the numerical results with the experimental test results by Alshaikh et al. [47]. Eight FE models with various specificities (a set of parameters) were studied considering material non-linearity to gain a deeper understanding of the progressive collapse.

2. Previous Experimental Study

Two experimentally-tested frames with detail shown in Figure 1 (i.e., NC-01 and RuC-01) from the research conducted by Alshaikh et al. [47] were chosen to validate the FE models of this study. The experimental tests were carried out to study the behavior of 1/3 scaled specimens with two concrete mixtures under progressive collapse. As shown in Figure 1, it was assumed that the middle column (failed column) had lost part of it while it was still loaded with gravity load. The first concrete mixture was normal concrete (NC), while the second mixture was rubberized concrete (RuC) which was made by replacing the fine aggregate (i.e., sand) with 20% of waste crumb rubber. Regarding the levels of crumb rubber replacement, studies reported that the reduction in the mechanical properties increased with increasing the replacement levels of rubber in the mixture and with preferably using replacement levels that are not more than 20%. In addition, the size of rubber particles must be between 1–2 mm to minimize reductions in mechanical properties [26,28,29,51]. The normal strength mixtures with a target cylinder compressive strength of 40 MPa at the age of 28 days and a maximum aggregate size of 10 mm were used. The concrete mixtures are summarized in Table 1. The experimental program, including design, fabrication, instrumentation, and testing methodology, can be found in the reference by Alshaikh et al. [47]. The FE models developed in the current research were verified using the experimental findings of the NC and RuC specimens tested by Alshaikh et al. [47].

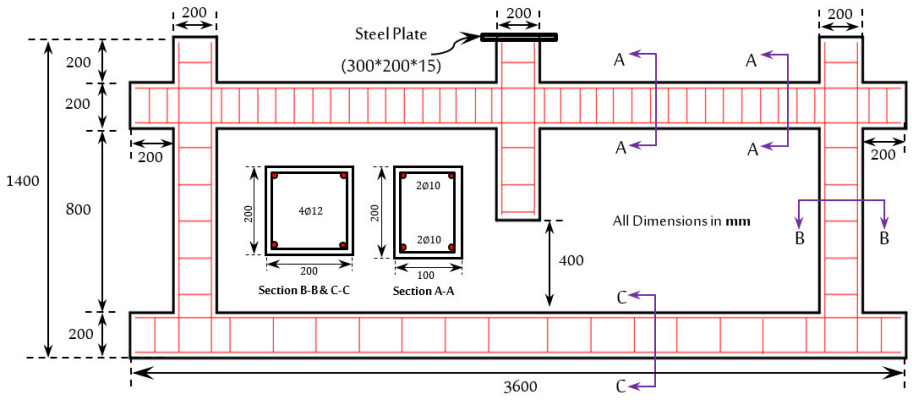

Figure 1. NC and RuC specimens details [47].

Table 1. Properties of NC and RuC mixtures [47].

Concrete Mixture	Cement	Water	Coarse Agg.	Fine Agg.	Crumb Rubber	Superplasticizer
NC (kg/m^3)	241.6	538.1	620.1	904.7	0	1.6 (liters)
RuC (kg/m^3)	241.6	538.1	620.1	723.7	51.5	1.6 (liters)

3. Details of the 3D RC Beam–Slab Substructures

The 10-story building considered in this study has a footprint of 3 bays by 4 bays, as illustrated in Figure 2. The story height is 3.0 m, while the bay span length in both orthogonal directions is 4.5 m, as depicted in Figure 2. The structure is situated in a non-earthquake zone. In addition, the RC building was designed according to ACI 318-11 [52], and ASCE [1] with the requirements of Category "A" for seismic design (i.e., the lowest seismic risk category). Uniform distributed load was applied to the slab surfaces for more realistic modelling. The living load and the superimposed dead load (i.e., tiles, ceiling, ducts, partitions, etc.) were 4.79 kN/m^2 and 2.0 kN/m^2, respectively, which were applied on floor slabs. The floor finishing loads were composed of four layers: (1) marble tiles with a thickness of 25 mm and a weight of 23 kN/m^3; (2) cement mortar with a thickness of 25 mm and a weight of 20 kN/m^3; (3) sand with a thickness of 50 mm and a weight of 18 kN/m^3; and (4) plaster with a thickness of 15 mm and a weight of 20 kN/m^3. A uniform distributed load of 8.7 kN/m was used to simulate the non-structural load (i.e., façade components), which affected all exterior RC beams. The façade components for the internal and external walls were carried out by two layers of 150 mm thick traditional concrete hollow-block with a weight of 17 kN/m^3 and 50 mm of thick rockwool with a weight of 0.5 kN/m^3. Considering the applying loads and the design standard requirements, the typical column and beam dimensions were 600 mm in depth by 600 mm in width and 600 mm in depth by 300 mm in width, respectively, on all the stories. Two-way solid slabs were designed with 120 mm in thickness for all the stories. After loading calculations and cross-section calculations for RC members, the commercial software ETABS (version 17) [53] was used in the structural analysis of this study to estimate all the influential forces on members (i.e., axial loads, shear forces, flexural bending moments). Figure 3 shows the structural analysis results of the influential forces on members. The longitudinal reinforcing rebars of columns were 8-T25 with reinforcement ratio, ρ of 1% and T10 stirrups at a spacing of 400 mm. The longitudinal rebars for positive and negative moments in beams consisted of 3-T16 with a reinforcement ratio of 0.3%, while the transverse rebars were T8 @ 250 mm along all the beam lengths. The longitudinal rebars for positive and negative moments in slabs consisted of 5-T10 per meter (i.e., T10 @ 200 mm spacing).

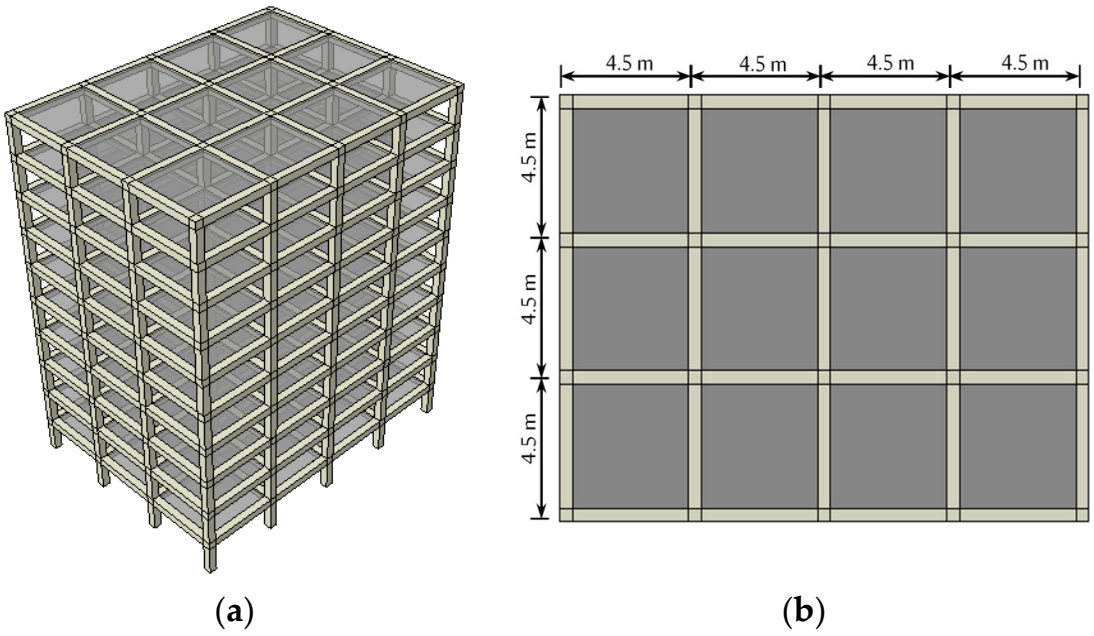

Figure 2. Typical plan and 3D view of the building considered in this study: (**a**) three-dimensional view; (**b**) floor plan.

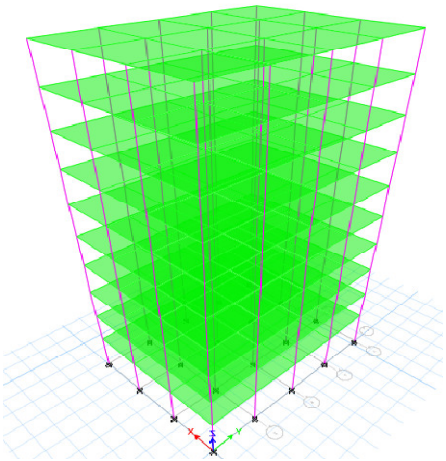

Figure 3. RC structure modelling by ETABS software.

4. FE Simulation Technique

The numerical analysis in this study was conducted using the commercial program ABAQUS-Explicit (version 6.19) [54] since it can model the nonlinear behavior of various materials and issues with complicated applications, both of which are required for this study.

4.1. Modelling of Concrete Materials

The concrete damaged plasticity model (CDP), which was available in ABAQUS software, was chosen to describe the concrete material performance which was commonly utilized in the FEM simulations (e.g., [43,44,49]). The CDP model can simulate the actual concrete behavior in compression and tension under external pressures. The CDP model was proposed by Lubliner et al. [55] as well as Lee and Fenves [56]. Before using the model, the dilation angle (ψ), the ratio of biaxial to uniaxial compressive strengths (σ_{b0}/σ_{c0}), compressive meridian (K_c), potential eccentricity (ϵ), and viscosity parameter (μ) required for ABAQUS modelling should all be specified. The parameters were chosen as recommended by Alshaikh et al. [49] and the ABAQUS User's Manual [54] as illustrated in Table 2. The modulus of elasticity (E_o) of NC and RuC mixtures was computed for the elastic component of the stress–strain relationship in accordance with ACI 318-11 recommendations [52] ($E_o = \rho_c^{1.5} 0.043 \sqrt{\sigma_c'}$, where ρ_c is the concrete density and σ_c' is the maximum compressive stress of a concrete cylinder) as summarized in Table 2. The Poisson's ratio (υ) of NC and RuC mixtures was taken as 0.2, which was commonly utilized in the FEM simulations [49].

Table 2. The primary parameters of the CDP material model used in this study.

Parameter	Value	Denotation
ψ	38 (calibrated value)	Alshaikh et al. [49]
ϵ	0.1 (default value)	ABAQUS [54]
σ_{b0}/σ_{c0}	1.16 (default value)	ABAQUS [54]; Lubliner et al. [55]
K_c	0.7 (default value)	ABAQUS [54]
μ	0 (default value)	ABAQUS [54]
Elasticity	Eo = 26,713 MPa for NC Eo = 20,704 MPa for RuC	ACI 318M-11 [52]
	υ = 0.2 for NC and RuC	Widely utilized in the FEM simulations

The stress–strain curve for the concrete uniaxial compression behavior can be separated into three zones, as shown in Figure 4. Up to a compressive stress of 0.4 σ_c', the first portion of the curve exhibits an ascending linear elastic behavior. Up until the maximum compressive stress, the second portion of the curve exhibits an increase in strain with the stress in a non-linear fashion. The third portion of the curve is characterized by a

non-linear softening model (i.e., declining) as a result of the decreased concrete capacity, as shown in Figure 4. For the non-linear FE studies, Hognestad [57] proposed a uniaxial compressive concrete model similar to that shown in Figure 4. Additionally, Stoner [58] modified the third portion of the curve shown in Figure 4 to take into account the impacts of maximum concrete strain and concrete confinement by stirrups. Figure 4 depicts the relationship between concrete compressive stress (σ_c) and concrete compressive strain (ε_c) with Equations (1)–(3) describing this relationship [57,58].

$$\sigma_c = \varepsilon_c E_o \qquad \text{for } \sigma_c \leq 0.4\,\sigma_c' \tag{1}$$

$$\sigma_c = \sigma_c'\left[2\left(\frac{\varepsilon_c}{\varepsilon_{c1}}\right) - \left(\frac{\varepsilon_c}{\varepsilon_{c1}}\right)^2\right] \qquad \text{for } \varepsilon_c/\varepsilon_{c1} \leq 1 \tag{2}$$

$$\sigma_c = \sigma_c' - \frac{\sigma_c'(\varepsilon_c - \varepsilon_{c1})^2}{(\varepsilon_{c,max} - \varepsilon_{c1})^2} \qquad \text{for } \varepsilon_c/\varepsilon_{c1} > 1 \tag{3}$$

where ε_{c1} = concrete crushing strain (i.e., strain corresponding to maximum concrete compressive stress; 0.00872 for NC and 0.0132 for RuC which were the experimental values); ε_c = concrete compressive strain; $\varepsilon_{c,max}$ = maximum concrete compression strain (0.01 for NC and 0.0151 for RuC which were the experimental values).

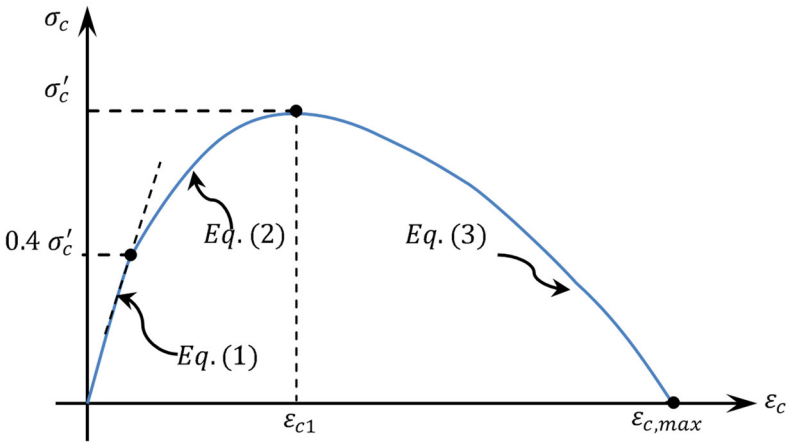

Figure 4. The σ_c–ε_c curve of concrete under compressive pressure.

Regarding modelling the tension behavior of concrete, until cracking stress the behavior is linear elastic (i.e., rising), then the non-linear stress–strain curve (i.e., softening) starts to descend due to the decrease in concrete strength as shown in Figure 5. The tension behavior of concrete is described by Equations (4) and (5) as described elsewhere [59].

$$\sigma_t = \varepsilon_{t1} E_o \qquad \text{for } \varepsilon_{t1} \leq \varepsilon_{cr} \tag{4}$$

$$\sigma_t = \sigma_{cr}\left(\frac{\varepsilon_{cr}}{\varepsilon_{t1}}\right)^{0.4} \qquad \text{for } \varepsilon_{t1} > \varepsilon_{cr} \tag{5}$$

where σ_t = tensile stress of concrete; σ_{cr} = cracking stress of concrete ($0.62\sqrt{\sigma_c'}$ according to ACI 318M-11 [52]); ε_{t1} = tensile strain of concrete; ε_{cr} = cracking strain of concrete (i.e., strain at σ_{cr}). The stress–strain curves, which were calculated according to the previous equations for the NC and RuC mixtures under compression and tension, are shown in Figure 6. As a result of the addition of crumb rubber (i.e., RuC), the strain increased even though the maximum stress decreased. It was also noted that the stress–strain curve had changed, as shown in Figure 6. The RuC specimen behaved differently than the NC specimen, displaying ductile behavior as opposed to brittle behavior for the NC specimen. The ductility increased as the crumb rubber was used. This behavior was deduced by contrasting the stress–strain curve shapes of RuC with those of NC. High deformations in

descending curves accompanied the RuC's failure state. The increased strain capacity of RuC bends was another distinction.

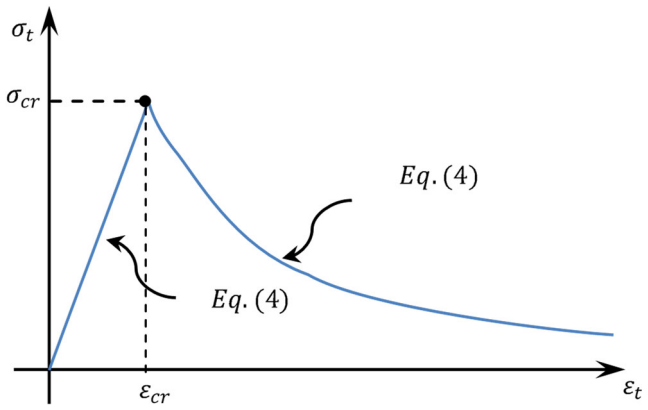

Figure 5. The σ_t–ε_t curve of concrete under tension.

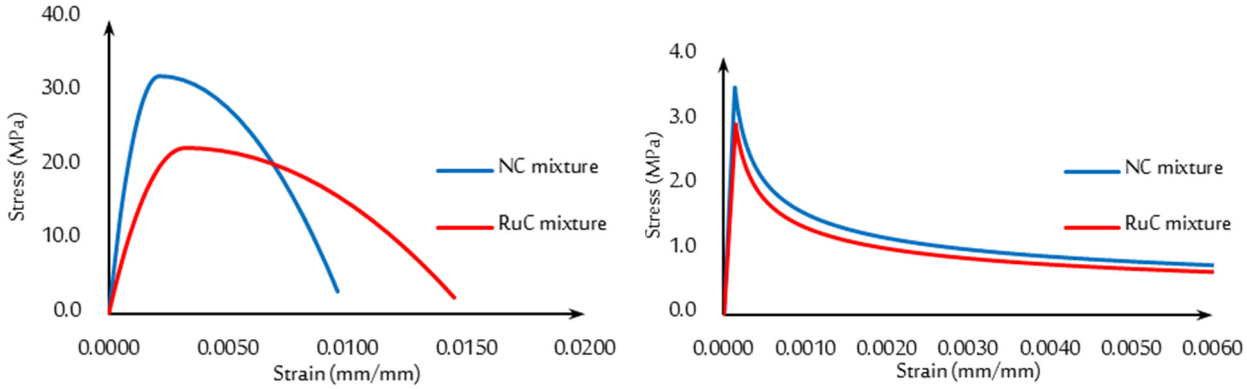

(**a**) (**b**)

Figure 6. Stress–strain curves of NC and RuC mixtures: (**a**) compression behavior and (**b**) tension behavior.

The determined elastic strain values must be converted to equivalent plastic strain values using Equations (6) and (7) in order to specify the concrete material in ABAQUS software [54], as follows:

$$\varepsilon_t^{pl} = \varepsilon_t^{el} - \frac{\sigma_t}{E_o} \quad (6)$$

$$\varepsilon_c^{pl} = \varepsilon_c^{el} - \frac{\sigma_c}{E_o} \quad (7)$$

where ε_c^{el} = compressive elastic strain (Figure 4); ε_c^{pl} = compressive plastic strain; ε_t^{pl} = tensile plastic strain; ε_t^{el} = tensile elastic strain (Figure 4).

A decline in stiffness and strength is referred to as material failure in a particular structure. Concrete can crack or crush during the loading phases, which results in the loss of the entire load-carrying capacity due to progressive degradation. The erosion algorithm method is utilized to simulate loss of stiffness in the progressive collapse operation and prevent computer overload during the calculation [60–63]. By using this approach, the model is able of capturing a more accurate graphic picture of how concrete physically fractures (i.e., cracks and crushes) after achieving its maximal strength. In addition, this algorithm can help the FEM simulation address the issue of a huge mesh-distortion by enabling the concrete finite components to erode, despite the fact that this is not a physics-based process. In other words, the physical separation of some finite elements from the rest of the mesh when the FE analysis produces excessive, improbable deformations and stops assisting with load resistance [36,63–65]. The erosion limitations and criteria

utilized in various research to simulate erosion and spalling in concrete were reviewed by Luccioni et al. [66]. The literature describes a number of erosion procedures, including principal stress, principal strain, shear strain, etc. Despite this, many erosion limit values are in agreement with the results of the experimental tests, the researchers advised expanded research on erosion limits due to a number of discrepancies in the literature that currently exist. To prevent inaccurate predictions from the numerical models caused by early erosion, which goes against the structure's mass and energy conservation, erosion limits must be utilized with prudence as a small limiting number. In order to accurately anticipate actual damage patterns that are comparable to the findings of experimental tests, an acceptable limiting value should be carefully chosen [60,63,64,67]. The maximum principal strain limitation value was determined based on the literature [62–65,67,68]. Calibrations using pertinent experimental tests are nevertheless necessary. As a result, numerous values were employed to test the validity of this value, and the results of the simulation and the experiment were compared. As a result, the concrete failure definition in ABAQUS software can be used to model the concrete failure criteria so that it accurately simulates the whole reaction of concrete. The ABAQUS software version of 2019 has added a new function known as the "Concrete Failure" keyword. Without utilizing subroutine functions, this keyword can be utilized to describe element deletion and failure criteria in the CDP model. Based on the tensile cracking displacement or tensile cracking strain, ABAQUS software allows the application of those two tensile failure criteria. The tensile cracking strain, which is determined by the cracking strain (i.e., tensile) and crushing inelastic (i.e., compressive) strain at failure, was used in this work. The values for the maximum principal strains according to the experimental results for the spalling and cracking of concrete were validated after a few trial-and-error calculations, as shown in Table 3.

Table 3. The primary parameters of the CDP material model used in this study.

Specimen ID	NC	RuC
Tensile cracking strain (mm/mm)	0.435	0.320
Compressive inelastic strain (mm/mm)	0.051	0.065

4.2. Modelling of Reinforcing Steel Rebars

Titoum et al. [69] proposed an idealized bi-linear stress–strain curve for simulating the reinforcing steel rebar behavior as shown in Figure 7. By giving the ultimate stress (σ_u), ultimate strain (ε_u), yield stress (σ_y), and yield strain (ε_y), the stress–strain response was created. For a numerical simulation, using the idealized curves is far more stable, therefore, it was used in this study. In accordance with ASTM A615 [70], experimental tests in tension were conducted to determine the characteristic values of the yield and ultimate stresses. These results are shown in Table 4. Using Hook's law, the modulus of elasticity (E_s) was computed as dividing the yield stress by the strain of reinforcing rebar. The Poisson's ratio for the reinforcing rebar was set as 0.3. Equations (8)–(10) were employed to convert experimental test results into true stress (σ_T) and true strain (ε_T) corresponding values in order to model the reinforcing rebar material in ABAQUS software [54,71]. Table 5 presents the stress and strain conversion values. Using the analytical equations below, the engineering stress and strain (i.e., σ_E and ε_E) were transformed to true stress and strain:

$$\varepsilon_T = \ln(1 + \varepsilon_E) \tag{8}$$

$$\sigma_T = \sigma_E(1 + \varepsilon_E) \tag{9}$$

$$\varepsilon^{pl} = \varepsilon^t - \varepsilon^{el} \tag{10}$$

where ε^{el} = true elastic strain; ε^t = true total strain; ε^{pl} = true plastic strain.

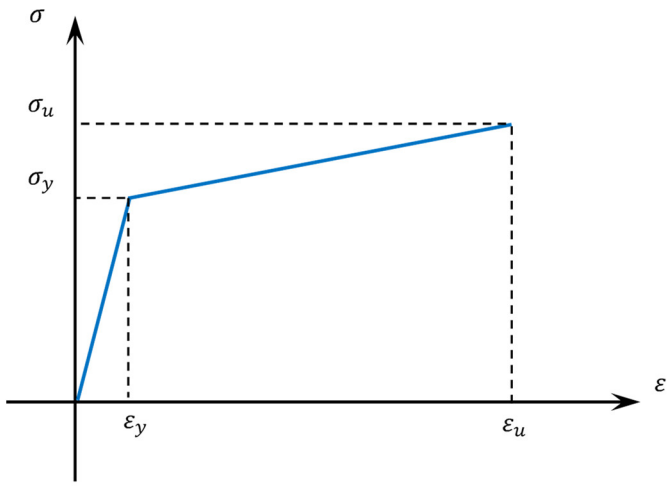

Figure 7. The idealized curve of σ-ε for reinforcing steel rebars.

Table 4. Reinforcing steel rebar material characteristics [47].

Rebar Diameter (mm)	E_s (MPa)	σ_y (MPa)	ε_y	σ_u (MPa)	ε_u
6	204,119	410	0.00201	507	0.0872
10	202,522	514	0.00254	625	0.1107
12	204,161	567	0.00278	653	0.1136

Table 5. Stress–strain conversions for reinforcing steel rebars.

Rebar Diameter (mm)		σ_E (MPa)	σ_T (MPa)	ε_E	ε_T	ε^{pl}
6	at yield	410	411	0.00201	0.00201	0
	at ultimate	507	515	0.08720	0.08360	0.0816
10	at yield	514	515	0.00254	0.00254	0
	at ultimate	625	695	0.11070	0.10500	0.102
12	at yield	567	569	0.00278	0.00278	0
	at ultimate	653	728	0.11360	0.10800	0.105

Additionally, fracture ductility was used to model the actual behavior of the reinforcing steel rebars in order to increase the accuracy of the FE analysis. Damage is a consequence of stress tri-axiality, and the commencement of damage is predicted by the fracture ductility criterion. Fracture stress and strain tri-axiality are the main determinants of ductile fracture. The mean stress (p) (i.e., hydrostatic stress) to the Von Mises stress (q) is the stress tri-axiality. According to Equations (11) and (12), which were proposed by Bridgman [72], the equivalent strain to fracture ($\bar{\varepsilon}_f$) and stress tri-axiality can be calculated.

$$\text{stress triaxiality} = \frac{p}{q} = \frac{1}{3} + \ln\left(\frac{a}{2R} + 1\right) \tag{11}$$

$$\bar{\varepsilon}_f = 2\ln\left(\frac{r_o}{a}\right) \tag{12}$$

where $q = \sqrt{1/2\left[(\sigma_1 - \sigma_2)^2 + (\sigma_2 - \sigma_3)^2 + (\sigma_3 - \sigma_1)^2\right]^2}$; $p = 1/3(\sigma_1 + \sigma_2 + \sigma_3)$; σ_1 = first principal stress; σ_2 = second principal stress; σ_3 = third principal stress; R = radius of circumferential notch (Figure 8); a = radius of rebar necking cross-section (see Figure 8); r_o = original radius of the reinforcing rebar.

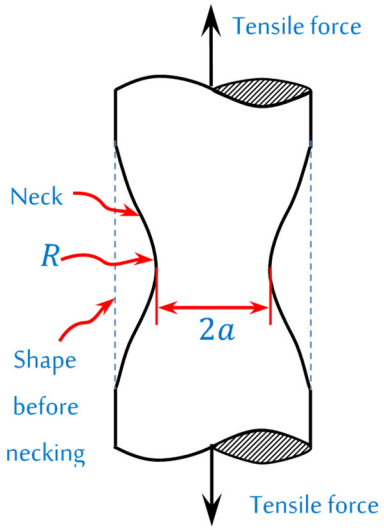

Figure 8. Necking of reinforcing steel rebar specimens under tension.

In order to improve the accuracy of ABAQUS FE simulation of reinforcing steel rebars, Bridgman's formulae [72] were used to determine the stress tri-axiality and $\bar{\varepsilon}_f$ of the longitudinal reinforcing rebars, as illustrated in Table 6.

Table 6. Stress tri-axiality and $\bar{\varepsilon}_f$ of steel rebars.

Rebar Diameter (mm)	R (mm) *	a (mm) *	r_o (mm)	Stress Tri-Axiality	$\bar{\varepsilon}_f$
10	8.02	2.55	10	0.481	1.347

* Experimental results based on tension testing of the reinforcing steel rebar [47].

4.3. Finite Elements

Continuum elements (i.e., solid cube-shaped) were utilized to model the RC members (i.e., beams, columns, and slabs) in each specimen. The element is known as C3D8R, which can be characterized as three-dimensional (3D), with 8 nodes, and with reduced integration to decrease the running time and significant computational power. Truss elements (i.e., T3D2) which can be characterized as 3D and 2-noded were used to model reinforcing steel rebars. The cross-sectional areas and diameters of all longitudinal and transverse reinforcing rebars were modeled in a comparable manner to the information provided by Alshaikh et al. [47].

4.4. Constraints and Interactions

A group of elements that are contained within the host elements can be referred to as the embedded elements with specific features. This method is specifically utilized to accurately recreate the bonding interaction between the reinforcing steel rebars and the surrounding concrete. By limiting the embedded elements' translational degrees of freedom to those in the host elements (i.e., surrounding concrete), the fully bonded condition was represented [54]. In the ABAQUS modelling, general contact was utilized to simulate the interactions between the middle column and the steel plate, shown in Figure 1, into a single interaction to define contact between them, in order to prevent the penetration of the steel plate and excessive distortion of the middle column (i.e., failed column). It is necessary to define the properties of the interaction in the ABAQUS modelling in order to accurately simulate the contact interactions. A friction coefficient of 0.47 between the steel plate and middle column surfaces was used to simulate the tangential behavior with no penetration of the surfaces (i.e., normal behavior), for the interaction properties in this investigation [73].

4.5. Boundary Conditions and Loading Application

Figure 9 shows specifics on the loading application and boundary conditions of all the specimens. A strip foundation was used in the experimental program to support the tested specimens in the laboratory. The strip foundation was not taken into account in the FE modelling because it requires more demanding computations, and it is assumed to be stiff enough to provide rigid support. Therefore, at the external columns' bottom surfaces, the supports were implemented by the fixed boundary condition for all rotations (UR) and translations (U) in all directions (i.e., URx, URy, URz, Ux, Uy, and Uz were restrained). By increasing the displacement at the top surface of the middle column (acting vertically downwards), the experimental loading was applied to the middle column until the entire test specimen failed.

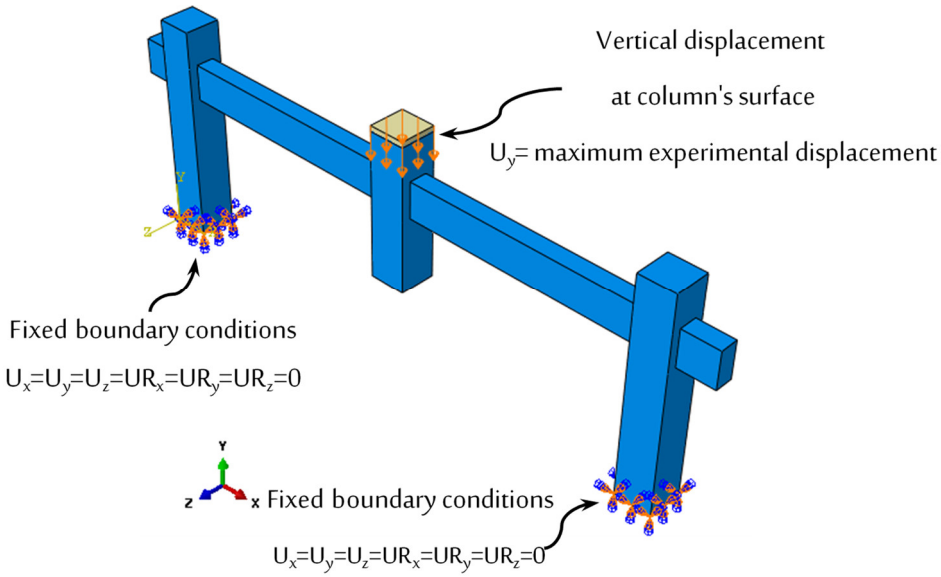

Figure 9. Boundary conditions and loading of tested frame specimens.

4.6. FE Mesh Convergence

In ABAQUS modelling, a 3D FE model of two concrete mixtures (i.e., NC and RuC frames) was created using the experimental data from Alshaikh et al. [47]. The steel plate at the load application was modeled using element type of C3D8R with elastic material characteristics only, E_s = 200,000 MPa and υ = 0.3. After modelling, only the NC frames were used for the mesh convergence investigation, which was done on three mesh sizes. The results are shown in Table 7. The geometry, material properties, and element types for all three mesh sizes were the same. With a uniform mesh size, which was utilized for reinforcing rebars and the remaining areas for columns and beams, the dense mesh size was employed in the beam–column connections (i.e., small mesh size in the critical sections near the connection and big mesh size in the remaining sections). To choose an appropriate mesh, a comparison of the three mesh sizes was conducted. In comparison to the experimental results, Mesh-size 3 with the greatest number of elements offered the greatest convergence and produced more accurate results, as shown in Table 7. Further mesh refinement effort needs more resources and running times with no convergence enhancement compared with the Mesh-size 3 results. As a result, all of the frames (i.e., NC and RuC) were made of the same size. The final target mesh (i.e., Mesh-size 3) is shown in Figure 10, where the complete frame included 1464 elements for the entire rebar reinforcement system and 9124 elements for the concrete components. There were 13,988 nodes produced in total throughout the entire frame.

Table 7. Mesh convergence results.

Mesh types	Element Type	Elements Number	$P_{Exp.}$ (kN)	$P_{FEM.}$ (kN)	$P_{Exp.}/P_{FEM}$	Running Time (s) *
Mesh-size 1	T3D2 C3D8R	532 764	53.293	58.133	0.92	720
Mesh-size 2	T3D2 C3D8R	692 980		57.521	0.93	960
Mesh-size 3	T3D2 C3D8R	1464 9124		56.782	0.94	4080

* Estimated operating time was based on a personal computer with 8.0 GB of RAM and a 2.5 GHz CORE i5 Quad-processor.

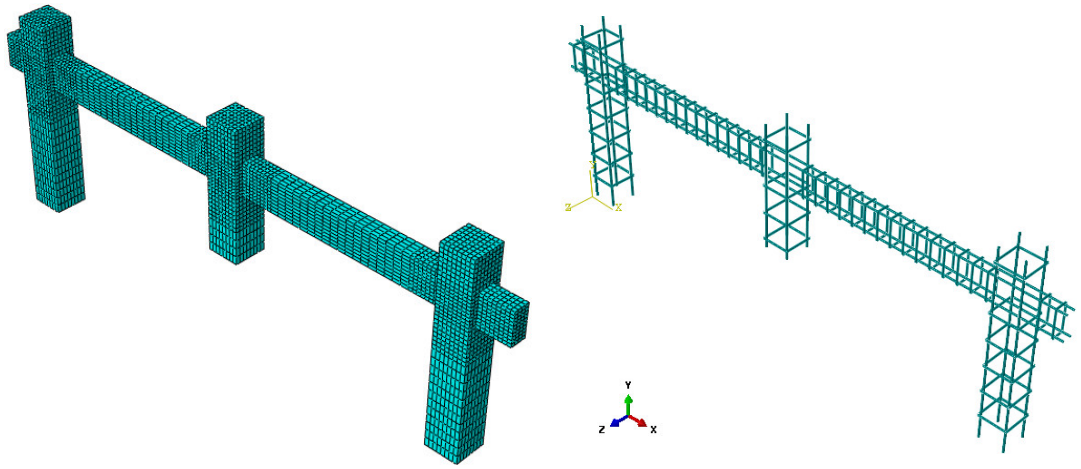

(**a**) (**b**)

Figure 10. Modelling of all frames in ABAQUS software: (**a**) element meshing and (**b**) reinforcing rebars.

5. Validation of Finite Element Modelling

The FE analysis produced extremely good results when compared to the results of the experimental tests. Table 8 compares the measured values of the experimental and numerical specimens, in terms of maximum loads (P_{max}), displacements (Δ_{max}), and the area under the load–deflection curve (i.e., E_u). The outcomes demonstrated the ability of the FE models to accurately simulate the response of the tested specimens. Regarding the load–deflection relationship shown in Figures 11 and 12, for the NC and RuC specimens, respectively, the FE simulation results agreed very well with the experimental findings. So, the whole load–deflection characteristic can be simulated by the FE for the NC and RuC frames. It is important to note that the CDP model does not allow for the graphical representation of crack formation. The authors who created this model [55], however, claimed that they made the assumption that cracking starts when the maximum principal plastic strain's (PE, Max Principal) sign is positive or the compressive equivalent strain (PEEQC) and tensile (PEEQT) values are greater than zero [54]. Figures 13 and 14 show that the experimental failure mechanism and fracture pattern exhibited in the NC and RuC specimens, respectively, matched the FE findings. Thorough explanation of the failure modes and crack pattern development of experimental specimens can be found in the publication by Alshaikh et al. [47]. According to crack patterns, the flexural failure mode was dominant in all the models. At the middle and ends of the two-bay specimens, flexural cracking started and expanded at tension fibers of the locations of maximum bending moments.

Table 8. Comparison of experimental and numerical load–displacement properties for the tested frames.

Specimen ID	Result	Experimental *	Numerical	Exp./Num.
NC	P_{max} (kN)	53.293	56.782	0.94
	Δ_{max} (mm)	137.82	137.01	1.01
	E_u (kN.mm)	6697.6	7070.03	0.95
RuC	P_{max} (kN)	48.274	53.985	0.894
	Δ_{max} (mm)	156.62	156.477	1.001
	E_u (kN.mm)	6851.1	7581.209	0.904

* E_u, Δ_{max}, and P_{max} were the experimental average values of two frames [47].

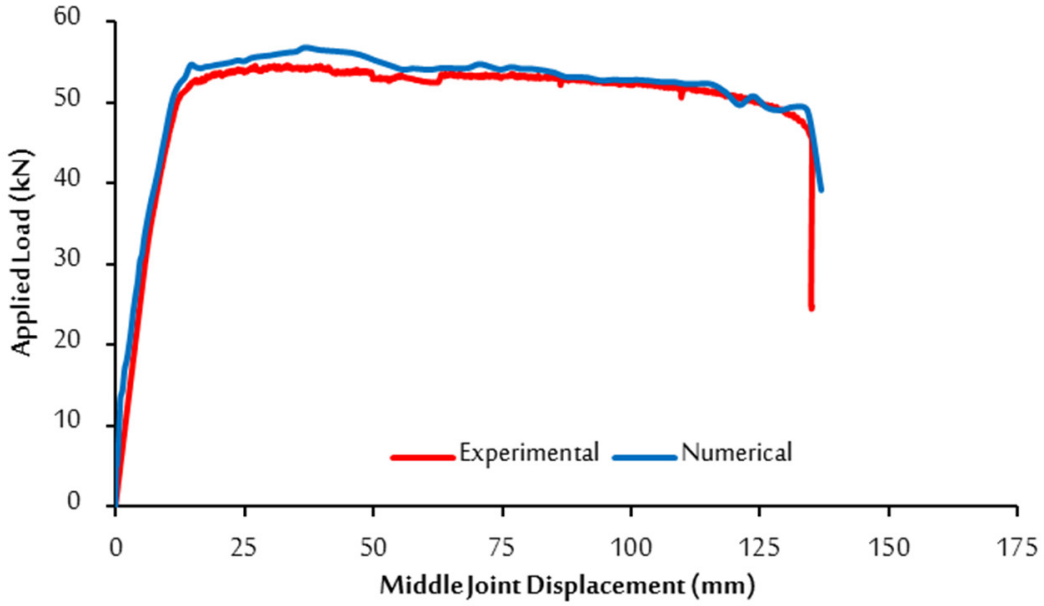

Figure 11. Comparison of the experimental and numerical load–displacement responses of the NC frames.

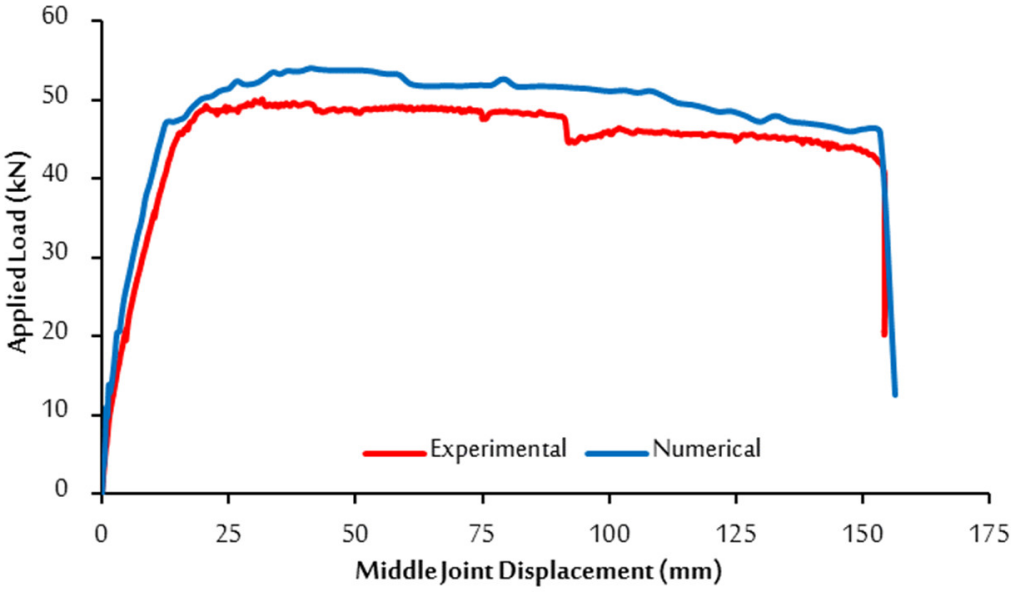

Figure 12. Comparison of the experimental and numerical load–displacement response of the RuC frame.

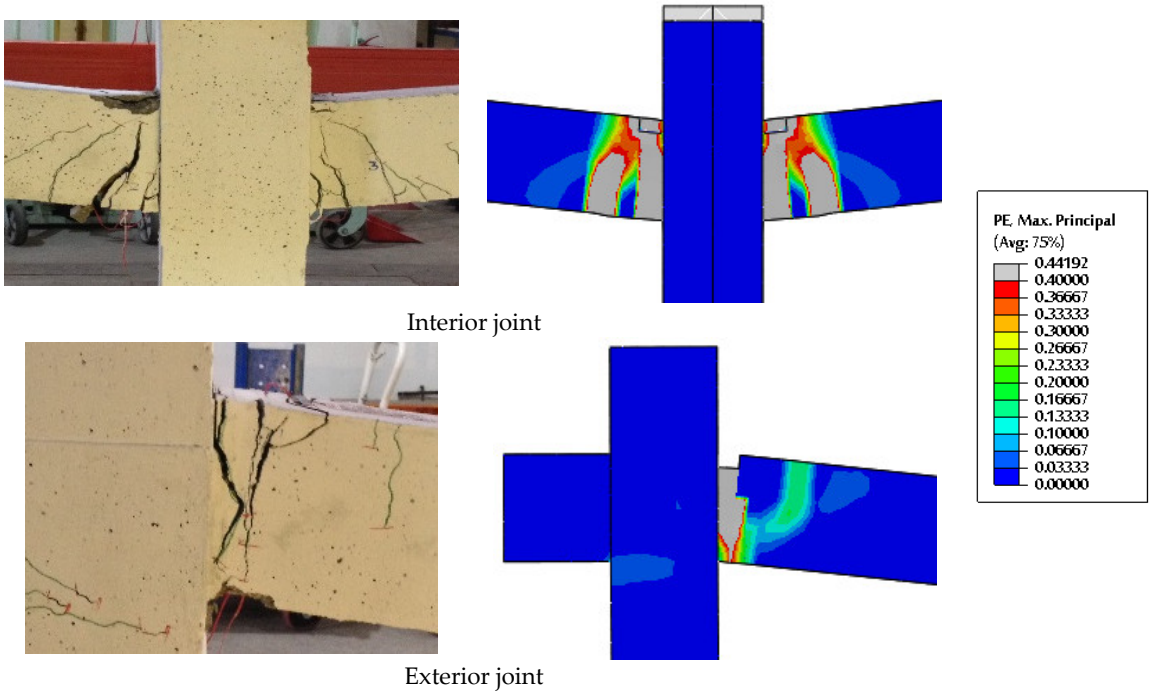

Figure 13. Comparisons of the experimental and FEM crack patterns for the NC frame at failure.

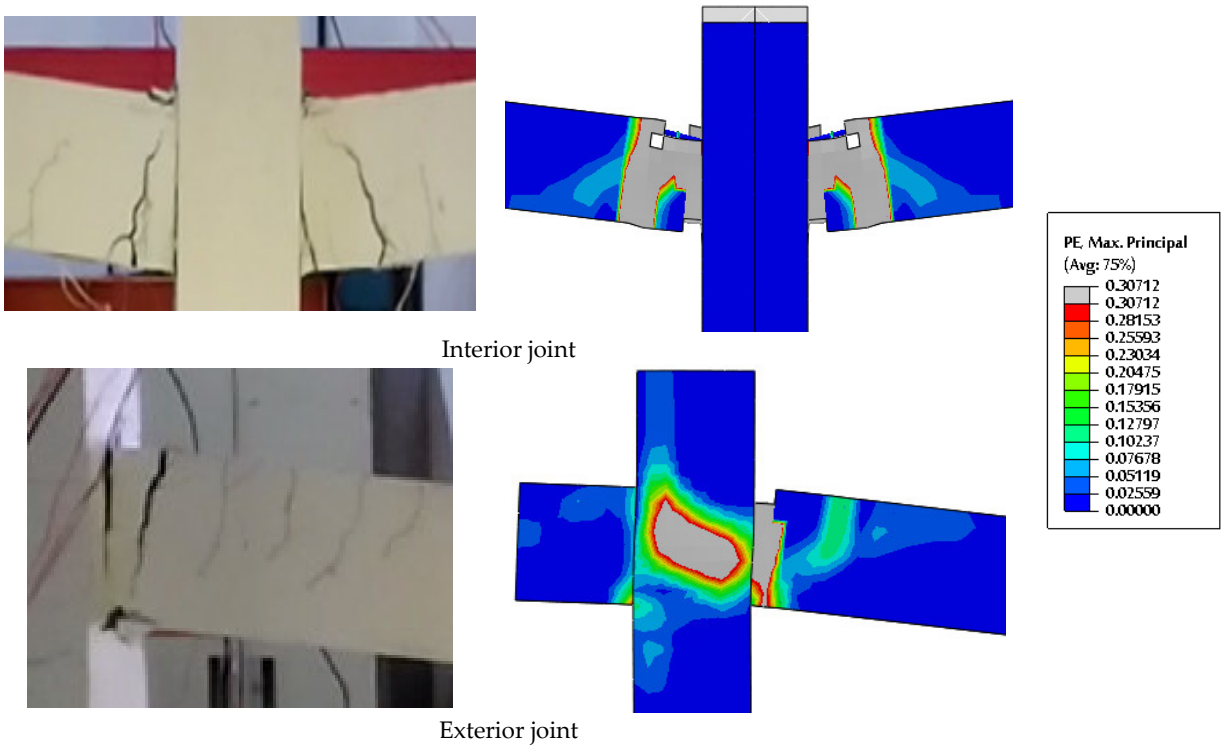

Figure 14. Comparisons of the experimental and FEM crack patterns of the RuC frame at failure.

6. Progressive Collapse Analysis of the 3D Beam–Slab Substructures

Eight FE models with various parameters were studied, utilizing the validated nonlinear FE model to gain a deeper understanding of their progressive collapse considering NC and RuC mixtures. To further understand the contribution of slabs to resist progressive collapse, specimens with and without these slabs were modeled. Table 9 presents a list of scenarios of the progressive collapse analysis that were taken into consideration in this study. Since they carry such heavy loads in comparison to other floors, the first-

story columns in the outer bays are possibly vulnerable to being destroyed by truck or car explosives. Therefore, this study focuses on investigating the effects of removing the first-story columns. Although the modelling of the whole structure is ideal to study the behavior of the structures under progressive collapse, conducting such analysis requires significant computational power and running times to obtain the results. This is due to the fact that modelling the complete structure would need a sizable number of finite elements, and given the available resources, modelling the full structure is not possible. Therefore, this numerical study focused on the most critical region in the entire structure. This technique was used in a lot of previous studies (e.g., [38,42,74]). Therefore, to decrease the significant analysis running time and computational power, the RC beam–slab substructures were modeled in ABAQUS as shown in Figure 15. The two scenarios of progressive collapse are being investigated. By removing the middle column in the structure's long direction as illustrated in Figure 15a, Scenario "A" has been implemented. By removing the corner column in the structure as illustrated in Figure 15b, Scenario "B" has been implemented. Figure 16 shows the reinforcement details of all the specimens of two scenarios of progressive collapse (i.e., A and B). The 3D beam–slab substructures were carried out following the FEM simulation techniques of the validated numerical model. In addition, the loads were applied in accordance with General Services Administration (GSA) guidelines [9] (2 dead load + 0.5 live load). The live load and the floor finishing load were taken as 4.79 kN/m^2 and 2.0 kN/m^2, respectively, which were applied on floor slabs as shown in Figure 17a,c. A uniform distributed load of 8.7 kN/m was used to simulate the non-structural loads (i.e., façade loads), which affected all the RC beams as shown in Figure 17b,d. Regarding the specimens without slabs, the slab loads were added to the non-structural façade loads and applied to all the RC beams. As seen in Figure 17a through Figure 17d, symmetrical boundary conditions in the YZ and XY planes were applied to all the specimens. In the ABAQUS software [54], the FE analysis of the specimens was divided into two steps. The total loads on all beams and slabs were initially applied in FE models as pressure loads on all beams' top surfaces and slabs (Figure 17). The results showed a considerable effect of the infill walls on the progressive collapse resistance that cannot be neglected [75]. Although the modelling of the infill walls is ideal to study the performance of the structures under progressive collapse, conducting such an analysis requires significant computational power, and it is time-consuming to obtain the results. According to the available resources, the infill walls could not be modeled. Therefore, this numerical study has focused on the slab contribution. This may lead to changes in the structural performance against progressive collapse, but it is beyond the scope of this study. By suddenly releasing the fixed support of the failed column (Figure 15), the two progressive collapse scenarios were applied in the second step. A vertical downward displacement of 700 mm was applied to the failed columns to understand the full resistance mechanism in the second step of analysis, as shown in Figure 17e. Figure 17f shows the mesh of the specimens, which were intensified in critical areas. The running time for the analysis of every FE model ranged from 4200 s to 22,440 s. It should be noted that the running time was estimated on a 2.5 GHz CORE i5 Quad-processor and random access memory (RAM) of 8.0 GB of the personal computer.

Table 9. Details of the FE analysis matrix for the 3D beam–slab substructures.

Scenarios	Specimen ID	Details	Mixtures	No. of Specimens
Scenario "A" (A middle column was removed)	NC-MID	without slab (see Figure 17a)	NC	1
	NC-MID-Slab	with slab (see Figure 17b)		1
	RuC-MID	without slab (see Figure 17a)	RuC	1
	RuC-MID-Slab	with slab (see Figure 17b)		1
Scenario "B" (A corner column was removed)	NC-COR	without slab (see Figure 17c)	NC	1
	NC-COR-Slab	with slab (see Figure 17d)		1
	RuC-COR	without slab (see Figure 17c)	RuC	1
	RuC-COR-Slab	with slab (see Figure 17d)		1
Total Specimens				8

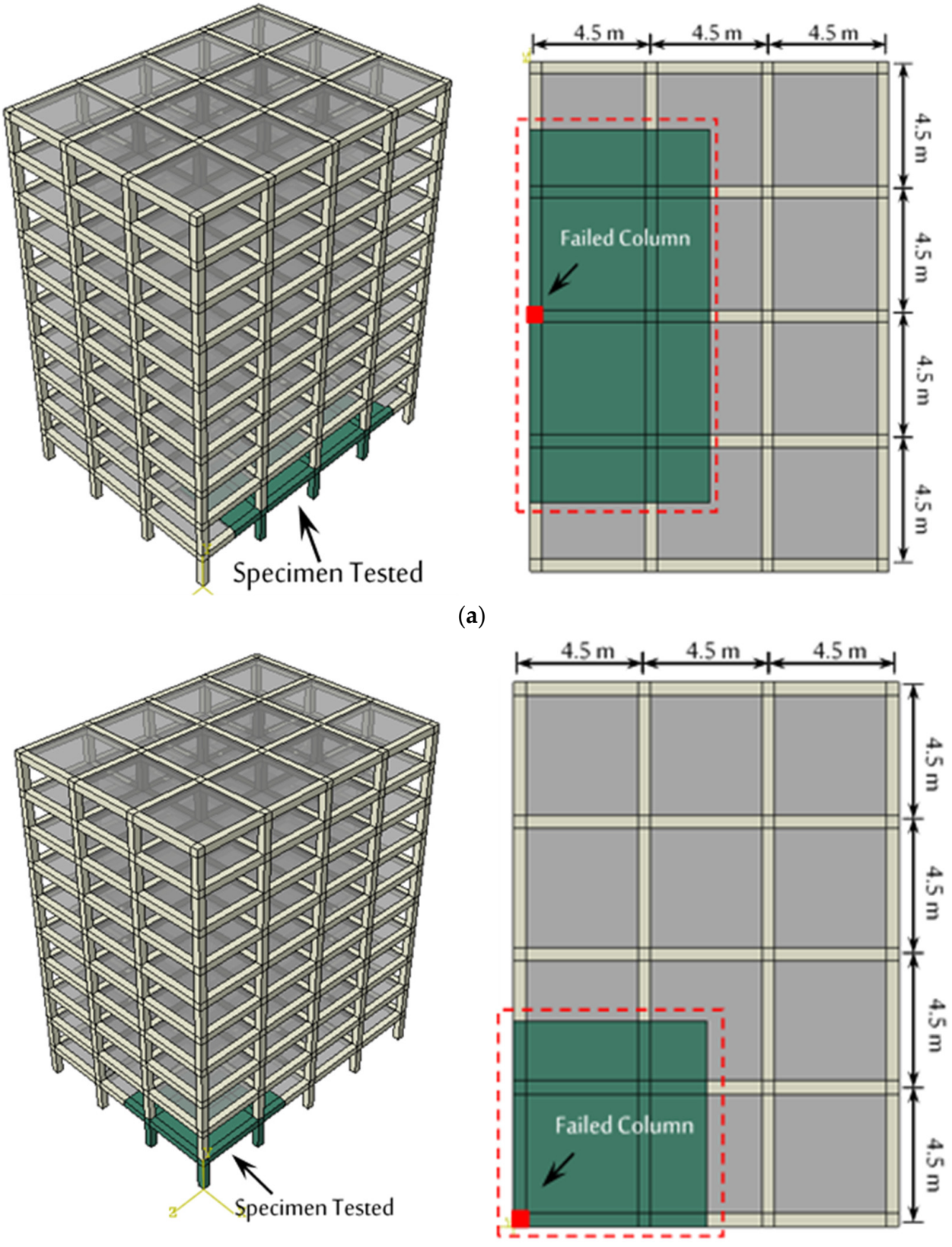

Figure 15. Beam–slab substructures used in the numerical study: (**a**) scenario "A" with middle column removed and (**b**) scenario "B" with corner column removed.

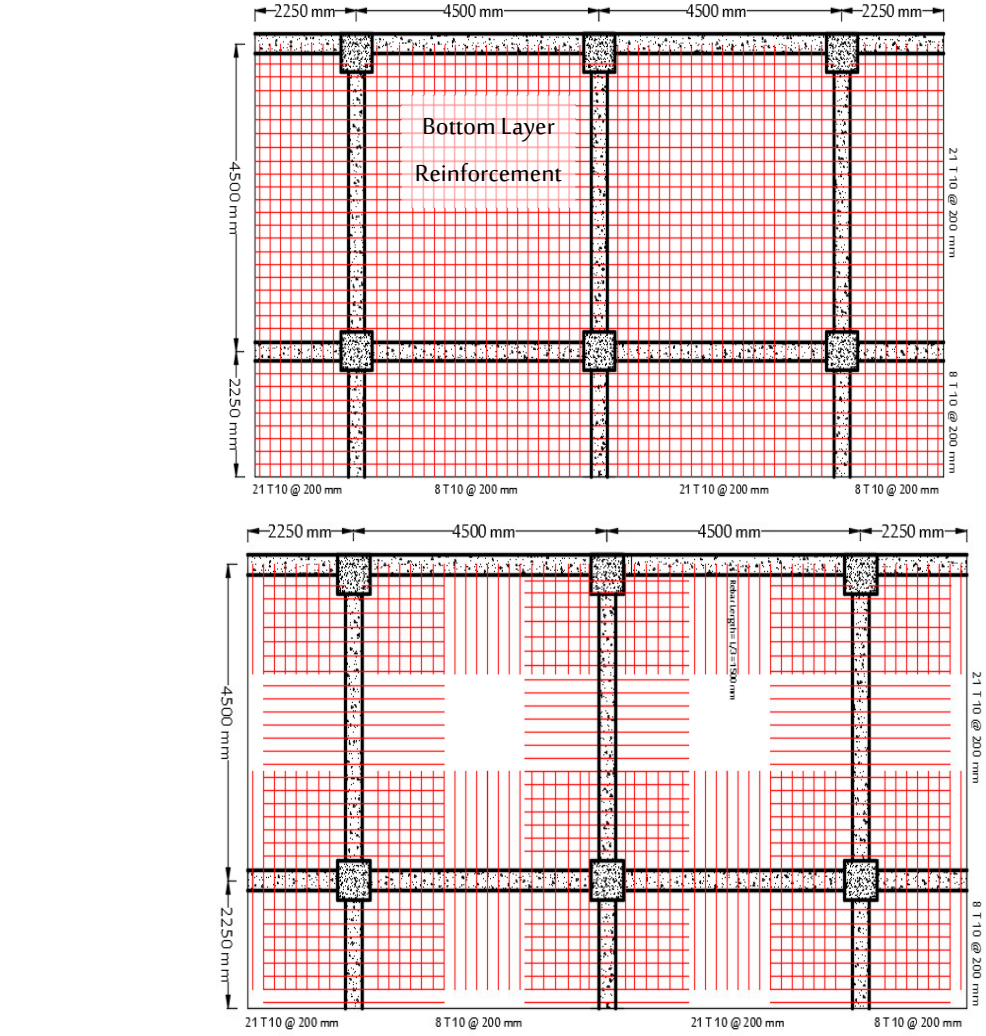

(**a**)

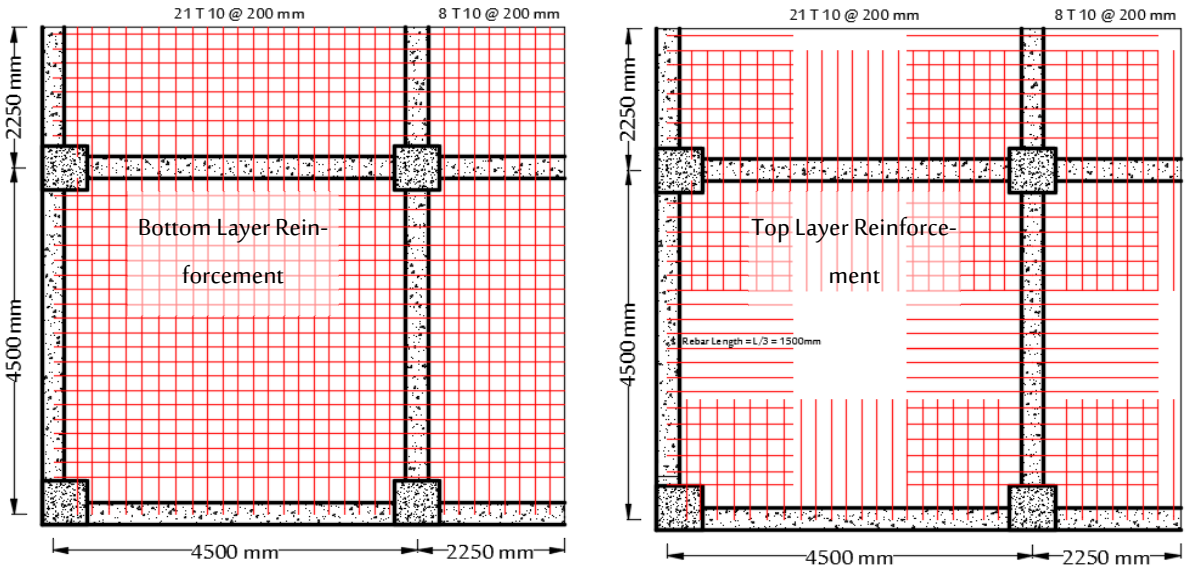

(**b**)

Figure 16. *Cont.*

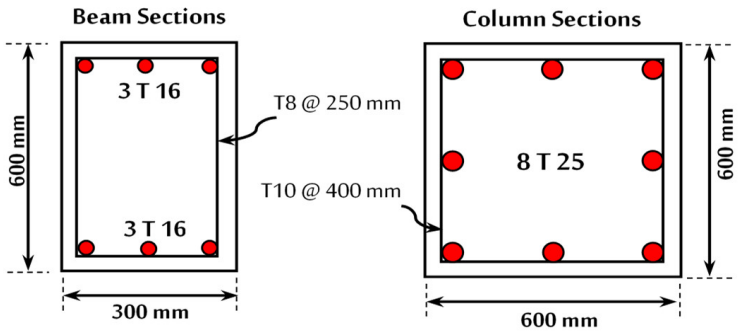

Figure 16. Reinforcement details of the specimens of the two frame scenarios of progressive collapse: (**a**) slab details of scenario "A"; (**b**) slab details of scenario "B"; and (**c**) beams and columns details.

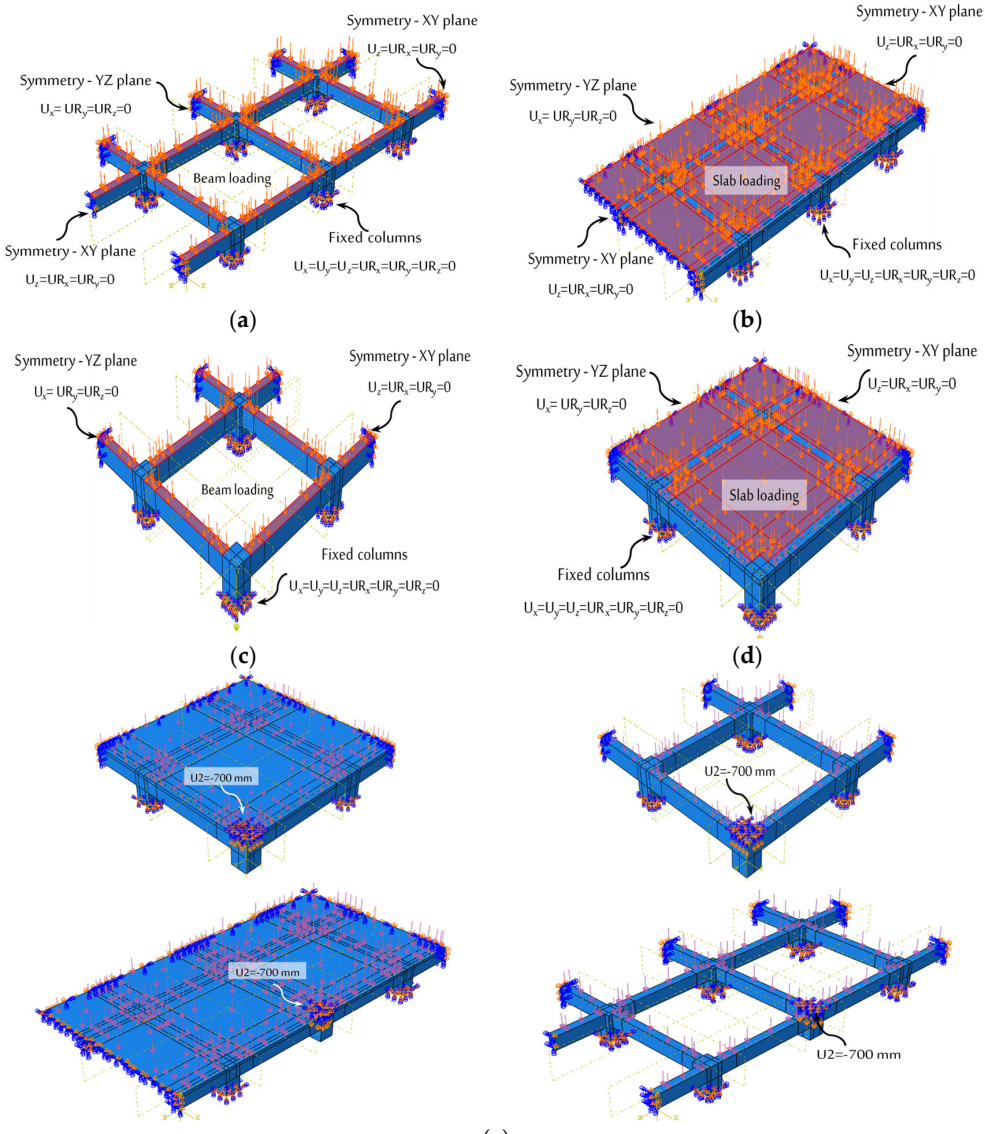

Figure 17. *Cont.*

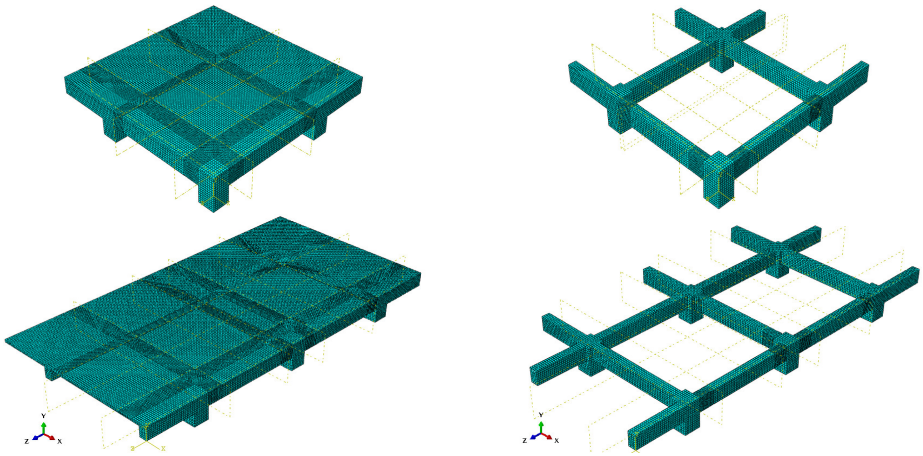

(**f**)

Figure 17. Assignment of loading and boundary conditions of all specimens: (**a**) NC-COR and RuC-COR; (**b**) NC-COR-Slab and RuC-COR-Slab; (**c**) NC-MID and RuC-MID; (**d**) NC-MID-Slab and RuC-MID-Slab, (**e**) applying of downward displacement; and (**f**) meshing of specimens.

6.1. Load–Displacement Characteristics

Figure 18 illustrates the vertical load and horizontal reaction force versus the vertical displacement of specimens of scenario A and B with and without a slab for various loading processes and resistance mechanisms. One may observe that the initial portion of the load–displacement curves is linear elastic, thus representing the uncracked concrete. After the start of concrete cracking, the slope of the load–displacement curves displayed non-linear behavior. All specimens continued to deflect while the applied load was increasing. The situation then remained unchanged until the reinforcing rebars yielded. A dramatic decrease in the resisting force was seen after the maximum vertical loads, as depicted in Figure 18. During the first analysis step (i.e., before removing the column), the vertical load increased to about 300 and 400 kN for the specimens of scenarios A and B, respectively, without any vertical displacement. In the second step of the analysis, it is noticed that the displacement begins to increase gradually with the increase of the vertical load as shown in Figure 18. The failure mode and crack pattern of all the specimens are shown in Figure 19. Regarding the scenario "A" specimens, the sections of the beams and slab close to the failed column were exposed to a positive flexural bending moment in the primary mechanism stage (i.e., the elastic stage), and the concrete began cracking at the bottom surface. Additionally, the areas of the beams and slab next to the neighbouring columns had a negative flexural bending moment, and the concrete began cracking at the top surface, as shown in Figure 19a through Figure 19d. For the scenario "B" specimens, the longitudinal reinforcing bar in the sections of the beams next to neighbouring columns started to experience fewer stresses as the joint flexural cracks widened, while the stresses on the bar in the sections of the beams close to the failed column increased quickly. This demonstrated the conversion of the specimen's resistance mechanism to a cantilever beam as shown in Figure 19e through Figure 19h. For scenario "B" specimens, pull-out failure was noticed in the top reinforcing rebars of beams in the beam–column joints at the failed column area. At the corner joint, the failed column was almost completely separated from the beams. The maximum vertical loads were 744.49, 647.73, 985.61, and 811.06 kN for NC-MID, RuC-MID, NC-MID-Slab, and RuC-MID-Slab, respectively, which were attained at a deflection of 40.55, 72.44, 40.55, and 40.53 mm for NC-MID, RuC-MID, NC-MID-Slab, and RuC-MID-Slab, respectively. Regarding the scenario "B" specimens, the maximum vertical loads were 692.34, 616.39, 978.51, 817.76 kN for NC-COR, RuC-COR, NC-COR-Slab, and RuC-COR-Slab, respectively, which were attained at a deflection of 42.59, 42.64, 43.26, and 43.79 mm for NC-COR, RuC-COR, NC-COR-Slab, and RuC-COR-Slab, respectively.

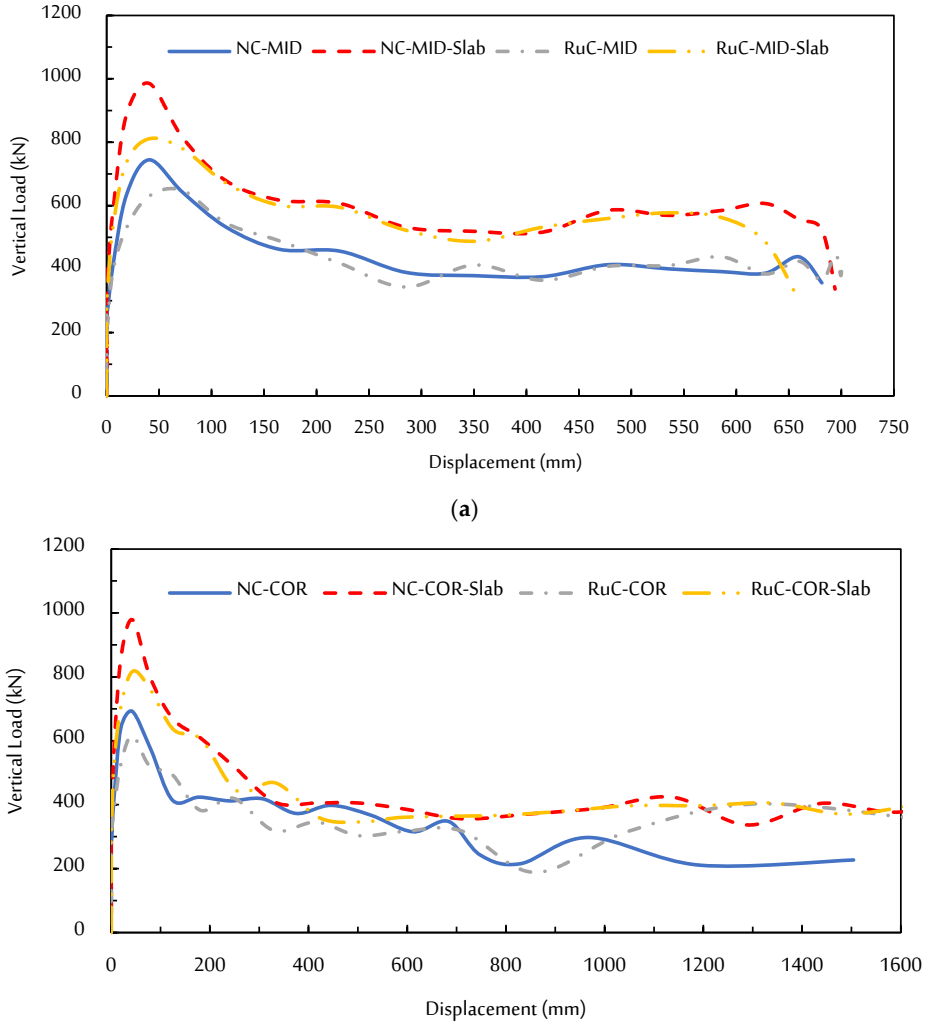

Figure 18. Vertical load–displacement curves: (**a**) Scenario "A" specimens and (**b**) Scenario "B" specimens.

6.2. Analysis of Collapse Mechanisms

Figure 20 shows the horizontal reaction force-displacement of all specimens, a negative horizontal reaction force indicates the specimens under compression force, and a positive horizontal reaction force indicates the specimens under tension force. The general failure behavior can be divided into three phases, namely: an elastic phase, compressive arch/membrane actions (CAA/CMA), and tensile catenary/membrane actions (TCA/TMA), as can be seen from the load–displacement responses of all specimens in Figure 20. The first stage (i.e., elastic stage) was during the uncracked concrete stage before the start of cracking. Then, after the concrete cracked, CAA/CMA was activated. The beginning of the catenary stage can be demonstrated by locating the point at which the horizontal reaction force equals zero, i.e., when the horizontal reaction force falls to zero and begins to transform from negative (i.e., compressive = CAA/CMA) to positive (i.e., tension = TCA/ TMA), as shown in Figure 20. The maximum capacities of all the specimens happened prior to the development of the TCA/TMA. The TCA and TMA forces (i.e., the catenary mechanism) in the longitudinal reinforcing rebars of the beams and slabs, respectively, were a major contributor to the progressive collapse resistance. Only the reinforcement of the slab and two-bay beams (in scenario "A") or perpendicular beams (in scenario "B") along the free edge considerably contributed to the resistance of the progressive collapse as a result of the boundary restrictions and the disproportionate deformation. The final damage state of all the all specimens is shown in Figure 21. As a result of the

start of concrete crushing in beams and slabs close to the failed column, the horizontal compressive reaction (CHR) increases nonlinearly, as shown in Figure 20. The maximum CHR for the specimens without a slab, NC-MID, RuC-MID, NC-COR, and RuC-COR, were −1036.24, −786.42, −1470.75, and −1164.32 kN, respectively, at a deflection of 72.47, 114.13, 42.59, 42.64 mm (see Figure 20). With increased deflection, severe cracks had developed near to the failed column, which caused the CHR to start to decrease. Concrete splitting was noticed in the end of beams, and concrete crushing increased in the two-bay beam as well as the transverse beam with a further increase in the deflection which led to failure in the area of column removal (see Figure 21a–d).

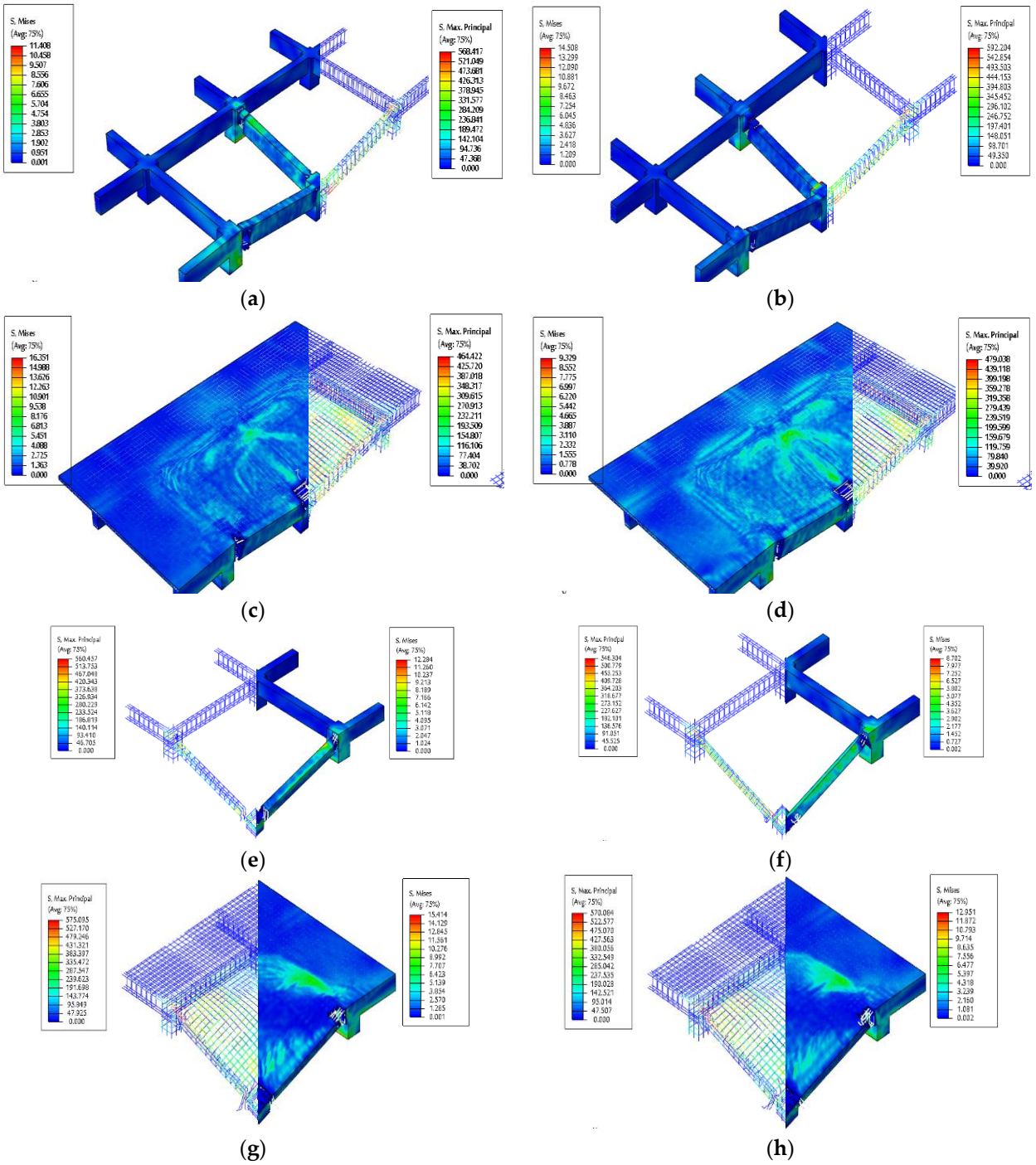

Figure 19. Failure mode and crack pattern for all specimens: (**a**) NC-MID; (**b**) RuC-MID; (**c**) NC-MID-Slab; (**d**) RuC-MID-Slab; (**e**) NC-COR; (**f**) RuC-COR; (**g**) NC-COR-Slab; and (**h**) RuC-COR-Slab.

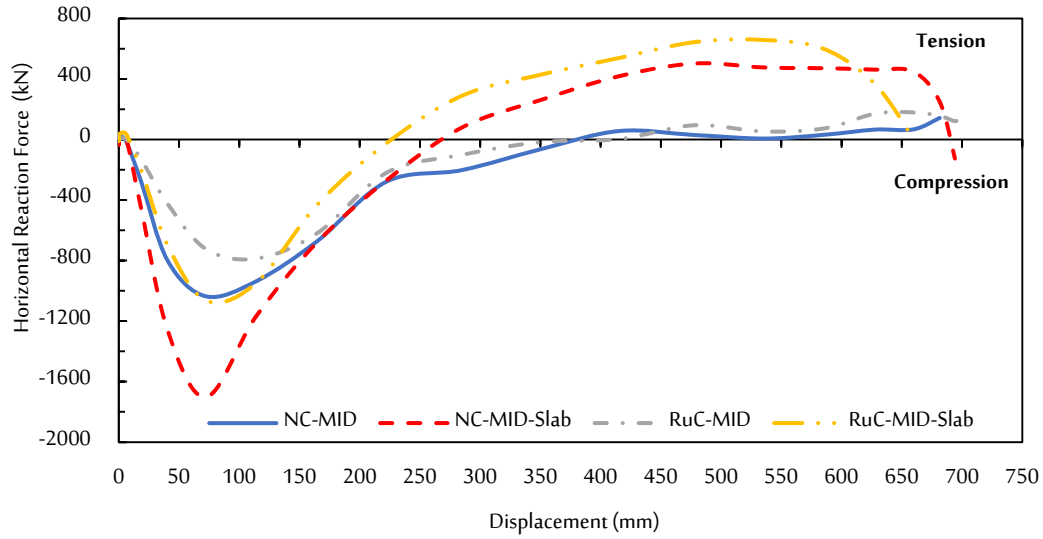

(**a**)

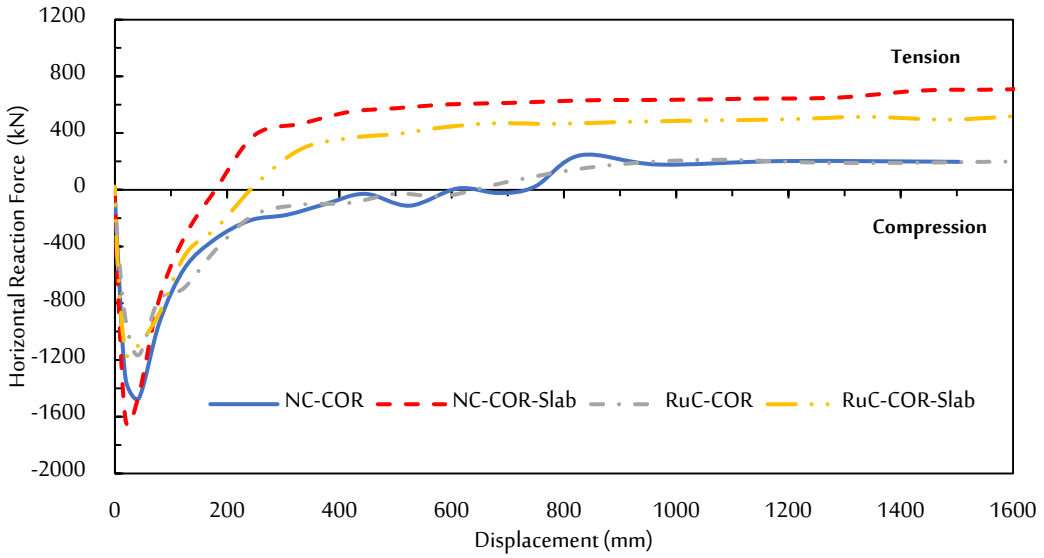

(**b**)

Figure 20. Horizontal reaction force–displacement curves: (**a**) Scenario "A" specimens and (**b**) Scenario "B" specimens.

Figure 22 illustrates comparison of the vertical load and horizontal reaction force versus the vertical displacement of the specimens. It can be observed that the specimens continued to resist until the stresses in the reinforcing steel reached the highest possible values (see Figure 19a,b,e,f); where the stresses reached more than 540 MPa at the ends of the two-bay beam as well as the ends of the transverse beam. Then, the bottom reinforcing rebars of the beams at failed column areas lost their collapse-resisting capacity. As a result, the top reinforcing rebars began to work as catenaries to carry the load and the TCA was activated, the same behavior has been reported in previous studies (e.g., [38]). The specimens were unable to maintain a greater level of collapse resistance, and the displacement was not permitted to increase continually. As shown in Figures 20 and 22, the resistance mechanisms have been changed from the horizontal compressive reaction (CHR) to the horizontal tensile reaction (THR) at deflections of 384.89, 405.87, 698.73, and 637.46 mm for NC-MID, RuC-MID, NC-COR, and RuC-COR, respectively. The maximum THRs were 142.89, 179.06, 244.17, and 211.41 kN, which were attained at deflections of 681.39 and 659.51 mm for NC-MID, RuC-MID, NC-COR, and RuC-COR, respectively.

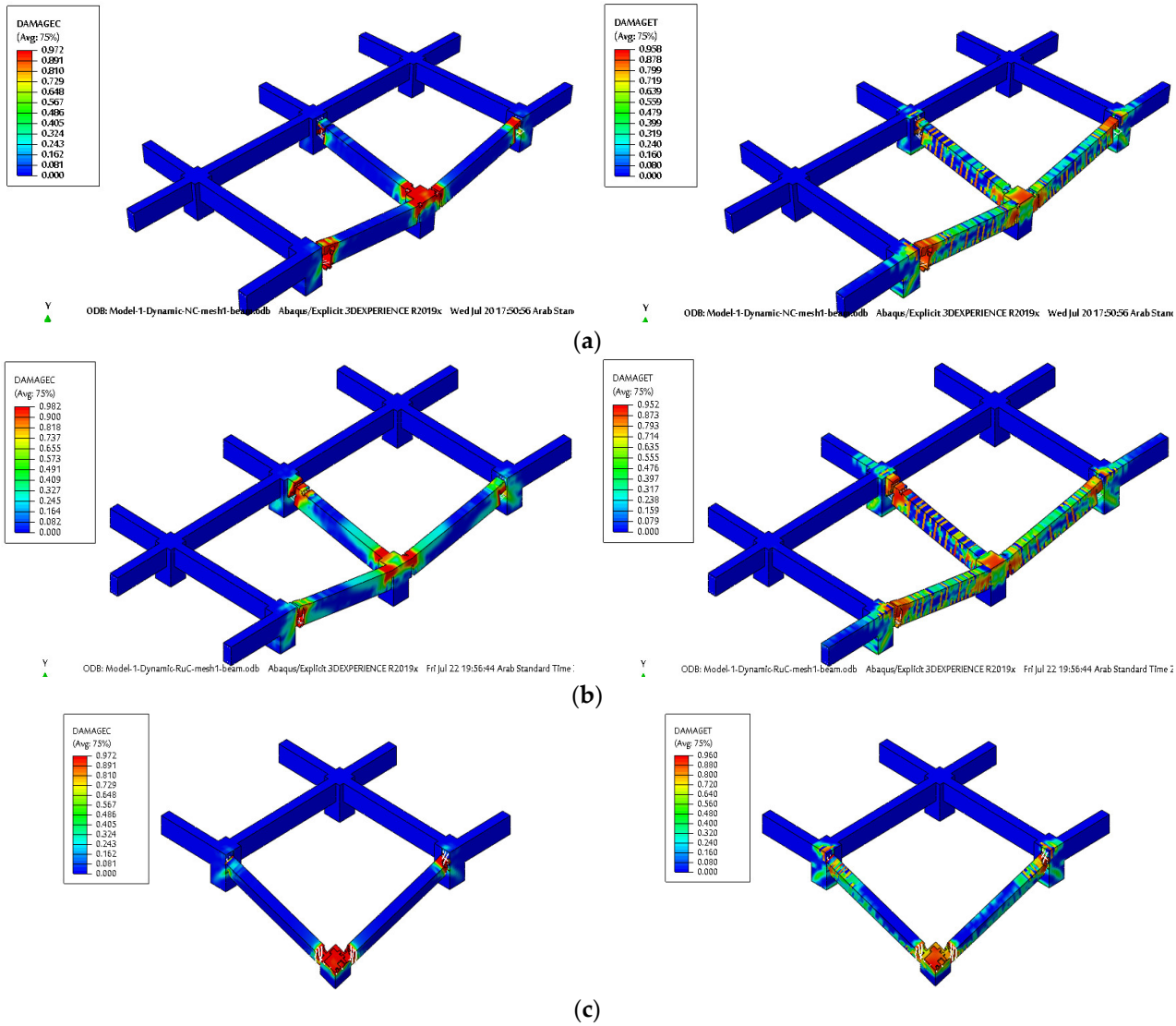

Figure 21. *Cont.*

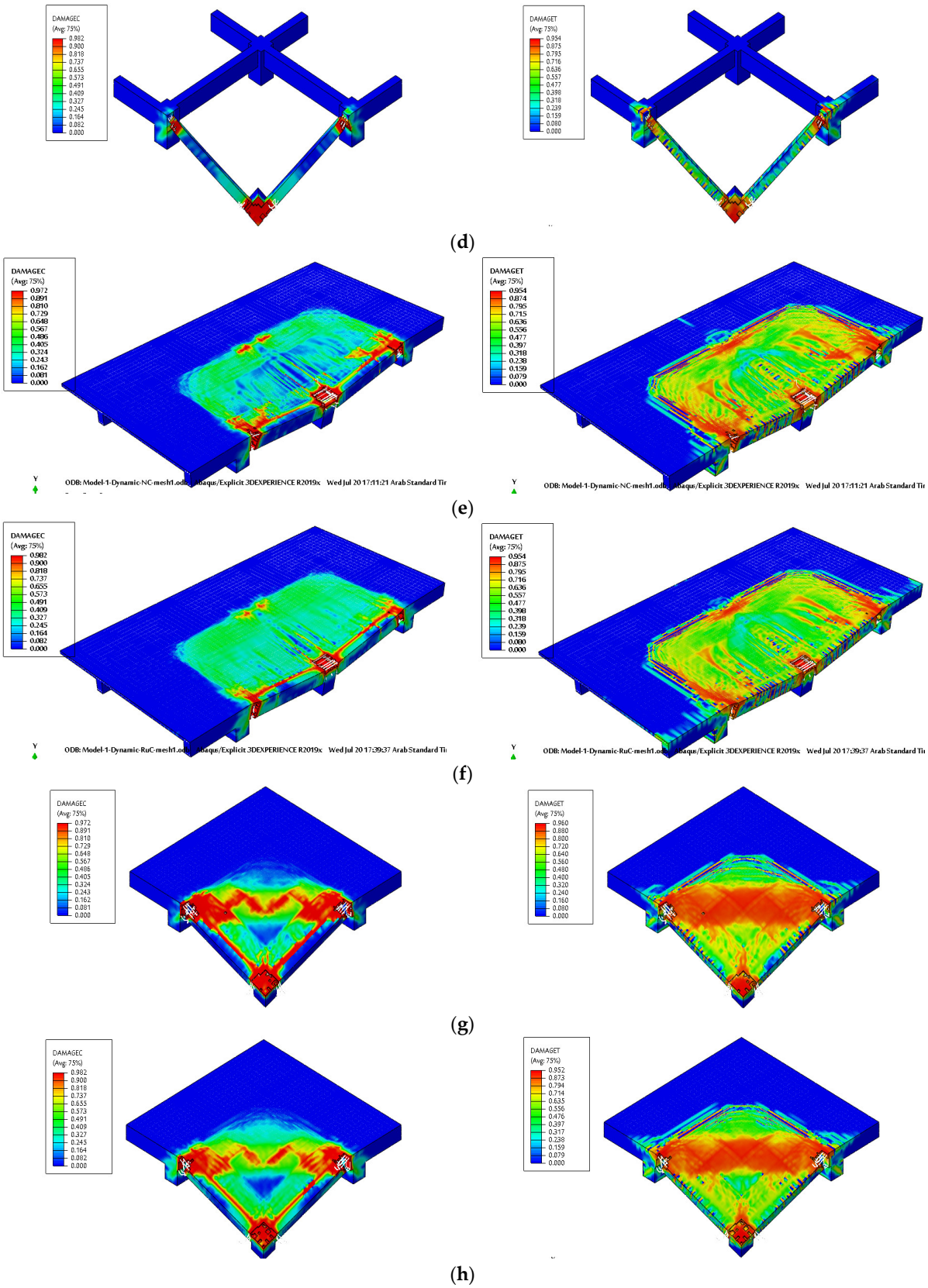

Figure 21. Concrete damages for all specimens: (**a**) NC-MID; (**b**) RuC-MID; (**c**) NC-COR; (**d**) RuC-COR; (**e**) NC-MID-Slab; (**f**) RuC-MID-Slab; (**g**) NC-COR-Slab; and (**h**) RuC-COR-Slab.

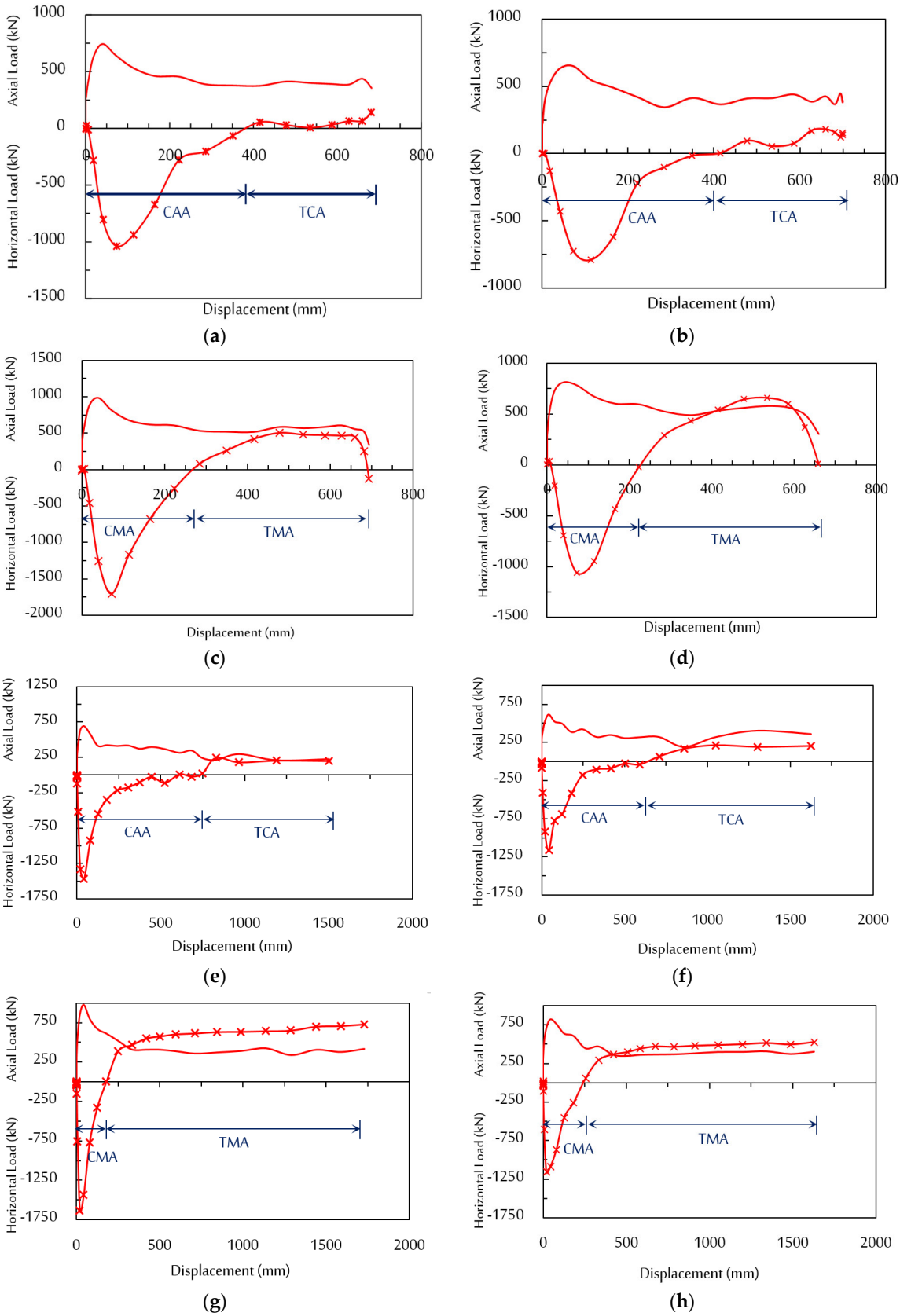

Figure 22. Load resistance mechanisms: (**a**) NC-MID; (**b**) RuC-MID; (**c**) NC-MID-Slab; (**d**) RuC-MID-Slab; (**e**) NC-COR; (**f**) RuC-COR; (**g**) NC-COR-Slab; and (**h**) RuC-COR-Slab.

Figure 21 shows the compressive concrete damage (i.e., DAMAGEC) and tension concrete damage (i.e., DAMAGET) forces. It was observed that the tensile and compressive damages gradually spread and were dispersed along the entire length of the beam in the two directions as the displacement was further increased (see Figure 21a–d)). Moreover, it was observed that the maximum CHR values were −1702.04, −1063.97, −1638.39, and −1158.67 kN for NC-MID-Slab, RuC-MID-Slab, NC-COR-Slab, and RuC-COR-Slab, at deflections of 72.47, 72.43, 19.92, and 43.79 mm, respectively, (see Figure 22c,d,g,h). With deflection increase, severe cracks had developed near to the failed column, which caused the CHR to start to decrease. Concrete splitting was noticed in the end beams, and concrete crushing increased in the two-bay beam as well as transverse beam with a further increase in the deflection. The specimens continued to resist until the stresses in the reinforcing steel reached the highest possible values (see Figure 19c,d,g,h); where the stresses reached more than 460 MPa at the ends of the two-bay beam as well as the ends of the transverse beam, then a drop in the vertical load resistance occurred to zero. First, the concrete cracks were seen near the failed column area, then the number of cracks gradually increased and expanded along a portion of the beam. On the top surfaces of the slab, ring cracks developed as depicted in Figure 23. The specimens were unable to maintain a greater level of collapse resistance, and the displacement was not permitted to increase continually. As shown in Figure 22c,d,g,h, the resistance mechanisms have been changed from CHR to THR at a deflection of 270.54, 227.06, 179.07, and 242.51 mm for NC-MID-Slab, RuC-MID-Slab, NC-COR-Slab, and RuC-COR-Slab, respectively. The maximum THR values were 502.55, 658.26, 730.13, and 527.24 kN, which were attained at a deflection of 477.81, 535.32, 1727.92, and 1629.45 mm for NC-MID-Slab, RuC-MID-Slab, NC-COR-Slab, and RuC-COR-Slab, respectively. As shown in Figure 21e–h, multiple cracks gradually spread throughout the entire slabs as a result of an increase in the displacement. Tensile and compressive damages gradually spread and were dispersed along the entire length of the beam in the two directions as the displacement was further increased (see Figure 21e–h). The damage was obvious on the top surface of the removed column. Under middle and corner column removal scenarios, Figure 23 depicts the distribution of the tension zone in the slab's centre and the compressive zone along the slab's sides as proposed by Pham et al. [76]. As shown in Figure 23a, a peripheral compressive ring formed around the TMA in the slab's centre in the middle-failed column case. In the case of a corner-failed column, as shown in Figure 23b, little TMA may be mobilized, and a peripheral compressive ring may still partially form. The results of the present study are in agreement with those of the previous one, especially the distribution of tensile (i.e., DAMAGET) and compressive (i.e., DAMAGEC) damages shown in Figure 21e–h. The intensity of lateral constraint given by a half-compressive ring of RC slab formed in the affected area determines the mobilization of catenary action. Catenary action continued to develop until the perimeter compressive ring failed in all specimens. As illustrated in Figure 23a, removing the middle column in the structure's long direction results in only a half-compressive ring (rather than a full ring), providing only a minimal amount of lateral constraint for any TMA mobilization. The most dangerous scenario for progressive collapse is when a corner column is removed because there are no longer any constraints from the two neighbouring sides of the failed column. The intensity of lateral constraint given by a quarter-compressive ring of the RC slab formed in the affected area determines the mobilization of catenary action as shown in Figure 23b.

6.3. Effect of Slabs against Progressive Collapse

Table 10 displays the most important test specimen results. The specimens without a slab had maximum vertical loads of 978.51, 817.76, 985.61, and 811.06 kN for NC-COR-Slab, RuC-COR-Slab, NC-MID-Slab, and RuC-MID-Slab, respectively, while the corresponding maximum vertical loads for specimens without slabs were 692.34, 616.39, 744.49, and 647.73 kN for for NC-COR, RuC-COR, NC-MID, and RuC-MID, respectively. This means that the capacity of the specimens with the inclusion of the slab mechanical properties in the modelling is an average of 33% greater than that for the specimens without the slabs.

This finding was the same as reported in previous studies (e.g., [74,77,78]). The area under the vertical load–displacement curves (i.e., energy absorption), is another indicator of the specimens' ability to resist progressive collapse. Regarding energy absorption, as shown in Table 10, the specimens with slabs exhibited higher potential for energy absorption, where NC-COR-Slab, RuC-COR-Slab, NC-MID-Slab, and RuC-MID-Slab have recorded increased energy absorption ratios of 55.6, 22.2, 38.5, and 23.9%, compared with NC-COR, RuC-COR, NC-MID, and RuC-MID, respectively. These findings indicate that the specimens without a slab were less ductile than the specimens with a slab. According to the findings, the presence of a slab increases the resistance to progressive collapse during the compressive arch stage and catenary action. In comparison to specimens without slabs (NC-COR, RuC-COR, NC-MID, and RuC-MID), the inclusion of slab mechanical properties in the FE modelling helps to increase progressive collapse resistance by 41.3%, 32.7%, 32.4%, and 25.2% under small deformations (i.e., the beam mechanism) and 58%, 28.5%, 16.1%, and 22.9% under large deformations (i.e., the catenary mechanism) for NC-COR-slab, RuC-COR-slab, NC-MID-slab, and RuC-MID-slab, respectively.

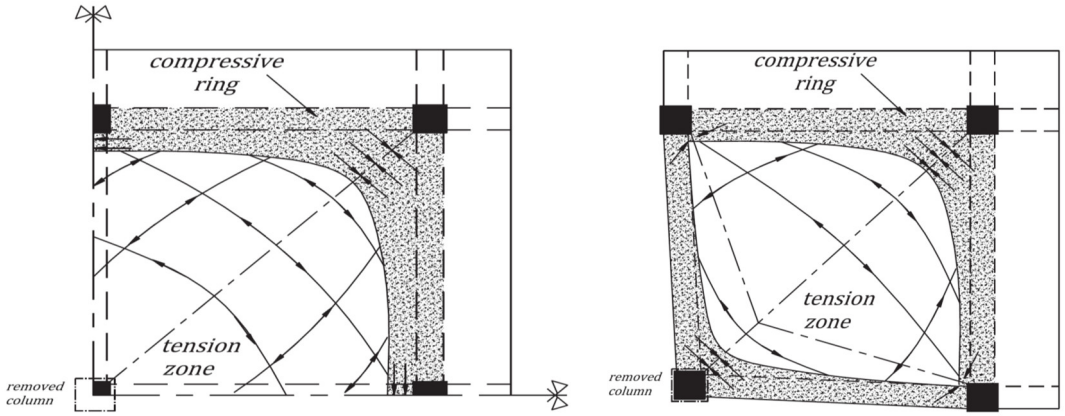

(**a**) (**b**)

Figure 23. Tensile membrane action (TMA) in RC slabs: (**a**) Internal failed column and (**b**) Corner failed column [76].

Table 10. Results of FE modelling for all specimens.

Specimen ID	Energy Absorption (kN.m)	Maximum Vertical Load (kN)	TMA/TCA Started (mm)	Maximum TMA/TCA (kN)	Maximum THR (kN)	Maximum CHR (kN)
NC-COR	483.06	692.34	698.73	423.72	244.17	−1470.75
RuC-COR	568.28	616.39	637.46	495.05	211.41	−1164.32
NC-COR-Slab	751.91	978.51	179.07	669.66	730.13	−1638.39
RuC-COR-Slab	694.25	817.76	242.51	636.01	527.24	−1158.67
NC-MID	304.34	744.49	384.89	531.76	142.89	−1036.24
RuC-MID	307.26	647.73	405.87	489.24	179.06	−786.42
NC-MID-Slab	421.62	985.61	270.54	617.51	502.55	−1702.04
RuC-MID-Slab	380.81	811.06	227.06	601.05	658.26	−1063.97

According to previous experimental research, when the slab contribution is taken into account, the first peak load of specimens (under small deformations) increases by 38–92%, while the maximum vertical load (under large deformations) increases by 40–145% [41,79,80]. Those results are consistent with the current study's findings. In addition, the slabs play an essential role in providing alternative paths for the failed column loads. These loads are redistributed to the adjacent columns, which are not taken into account if the presence of the slabs is ignored. The load resistance from the CMA in the slab contributed more as the displacement increased. Together, the CMA of the slab and the CAA of the beam considerably increased the structure's ability to resist progressive collapse under the main mechanism.

Regarding scenario "B" specimens, the NC-COR-Slab exhibited greater horizontal compressive reaction force by 11.4% compared with the NC-COR, while RuC-COR-Slab recorded a slight reduction by 0.5% compared with the RuC-COR. Moreover, scenario "A" specimens NC-MID-Slab and RuC-MID-Slab have recorded significantly increased ratios by 64.4% and 35.3%, compared with NC-MID and RuC-MID, respectively. Due to the TMA of the slabs and the TCA of the beams, the progressive collapse resistance increased once again. The specimens with slabs exhibited higher potential for horizontal tensile reaction force, where NC-COR-Slab, RuC-COR-Slab, NC-MID-Slab, and RuC-MID-Slab have recorded increased ratios by 199.0, 149.4, 251.7, and 267.6%, compared with NC-COR, RuC-COR, NC-MID, and RuC-MID, respectively. As the two-bay beams (in scenario "A") or perpendicular beams (in scenario "B") moved downward, they started to rotate about their longitudinal axis as a result of torsion effects. The effect of torsion appears significantly in the perpendicular beam (in scenario "B" specimens), which works as a cantilever beam as shown in Figure 24, which weakens the specimen's resistance to progressive collapse. The combined bending and torsion effects create diagonal cracks in the beams. The presence of the slabs led to a change in the performance of the beams, which provided additional constraints and allowed for a reduction in the effect of torsion on the beams. This means that the slabs cannot be dispensed in the progressive collapse testing of RC structures because of their significant ability to improve the progressive collapse resistance of RC structures.

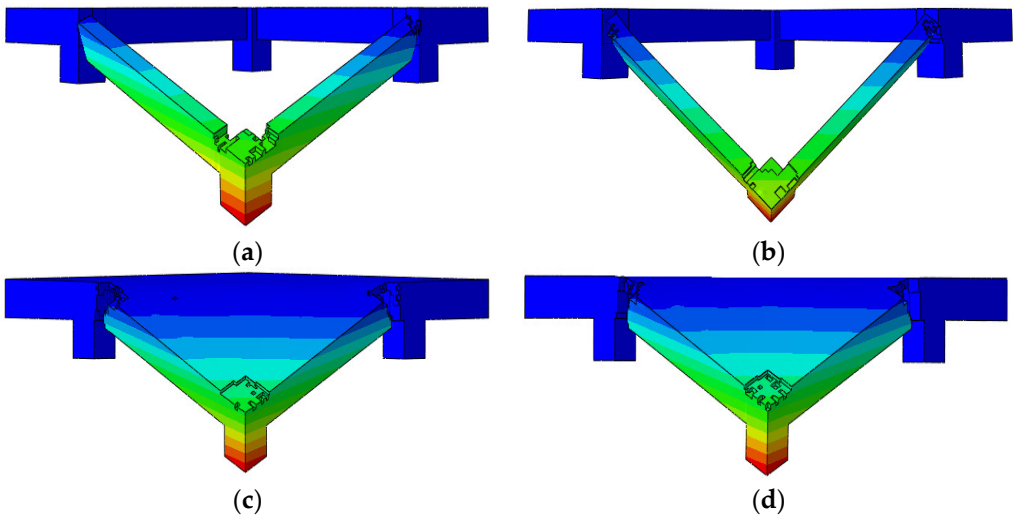

Figure 24. Torsion effects on in scenario "B" specimens: (**a**) NC-COR; (**b**) RuC-COR; (**c**) NC-COR-Slab; and (**d**) RuC-COR-Slab.

6.4. Effectiveness of the Use of Rubberized Concrete

Four RuC specimens with and without slabs were tested where the fine aggregate (i.e., sand) in the RuC mixtures was partially replaced by crumb rubber using 20% of the sand volume. Regarding the specimens without a slab, it is noted that the damages are more widespread in RuC specimens than in NC specimens (see Figure 21a–d). However, slight differences were recorded in the maximum vertical load, with a reduction ratio between 12% to 15% for RuC specimens compared with NC specimens. Regarding the specimens with a slab, a significant difference was recorded in the maximum vertical load, with a reduction ratio between 19% to 21% for RuC specimens compared with NC specimens (see Figure 22g–h). The increase in the percentage compared to the specimens without slabs can be attributed to the fact that the RuC mixture has been used in the slabs (i.e., RuC-MID-Slab and RuC-COR-Slab) and that the compressive strength of RuC is less than that of the NC mixture. Concrete's compressive strength can be quite important, especially for the seismic performance of RC structures [81]. Regarding energy absorption, for specimens without slabs, the RuC specimens recorded an increase in energy absorption of 0.96% for RuC-MID

compared with NC-MID and 17.64% for RuC-COR compared with NC-COR. However, the opposite happened in specimens with specific slabs (i.e., NC-MID-Slab and RuC-MID-Slab). NC-MID-Slab recorded an energy absorption increase ratio of 10.7% more than RuC-MID-Slab, and NC-COR-Slab exhibited an increase ratio of 8.3% compared with RuC-COR-Slab. Despite the low load carrying capacities in the RuC specimens, it showed an ability to absorb energy more than or close to the NC specimens. Crumb rubber aggregates typically exhibit greater strain at the time of fracture because they have the capacity to withstand significant elastic deformation before failure. With the inclusion of crumb rubber, the failure of RuC specimen becomes more gradual due to crumb rubber's capacity to absorb significant amounts of energy under compressive and tensile pressures [50,82,83].

The significant differences between the NC and RuC mixtures appeared in the CAA/CMA stage, while no significant differences were observed in the TCA/TMA stage. The distribution of DAMAGEC and DAMAGET in the RuC specimens was more than the NC specimens, which can explain the decrease in measured vertical load capacity and CAA/CMA. Regarding the specimens with slabs, NC-MID-Slab and NC-COR-Slab showed slight increases in TMA forces of only 2.7% and 5.3% compared to RuC-MID-Slab and RuC-COR-Slab, respectively. While in the specimens without slabs, RuC-COR showed TCA force more than NC-COR by 16.8%, and the opposite for RuC-MID, which recorded a slight reduction ratio by 8.7% compared with NC-MID. This can be explained by the fact that the compressive strength is an important factor in the development of CAA/CMA, and the compressive strength in the RuC mixture was less than that of the NC mixture, and thus the remarkable superiority of NC specimens appeared. As for TCA/TMA, the reinforcing rebar plays an important role in the development of TCA/TMA, and since reinforcing rebar is equal in the two mixture specimens, no significant differences appeared between the two mixtures.

7. Conclusions

Based on the reported numerical results, the following conclusions can be drawn:

1. The FE simulation model produced extremely satisfactory findings in comparison with the available experimental test results in the literature for the load–displacement characteristics, crack patterns, and failure modes. It successfully addressed the majority of the issues relating to time savings, cost savings, and the potential risk of progressive collapse in experimental tests of the 3D beam–slab substructures.
2. The inclusion of the slab mechanical properties in the FE modelling increased the load resistance by an average of 33% for the tested specimens, and it also improves the frame's stiffness, ductility, and integrity. Moreover, the specimens with slabs exhibited higher potential for energy absorption, which reached up to 55%.
3. Compared to the specimens without slabs, the specimens with slabs have significantly higher progressive collapse resistance. The increase ratios reached up to 40% under small deformations (i.e., the beam mechanism) and up to 58% under large deformations (i.e., the catenary mechanism).
4. Compared to NC specimens, the RuC specimens recorded a reduction in the maximum vertical load as a result of lower compressive strength and modulus of elasticity. The reduction ratio reached up to 21% and 15% for RuC specimens with and without slabs, respectively.
5. Comparing the energy absorption of RuC specimens, it was found that NC specimens recorded a slight increase in energy absorption that reached up to 10.7% in the case of presence slabs, while RuC specimens recorded an increase in energy absorption that reached up to 17.6% in the case of absence slabs.
6. The significant differences between the NC and RuC mixture appeared in the CAA/CMA stage, in which the distribution of DAMAGEC and DAMAGET in the RuC specimens was more than those for the NC specimens. However, no significant differences between the two mixtures were observed in the TCA/TMA stage.
7. Despite the low load-carrying capacities of the RuC specimens, they showed an ability to absorb energy more than or close to the NC specimens. Moreover, the performance

of the RuC specimens was excellent in the TCA/TMA stage, which is the last line of defense against progressive collapse, and which develops additional resilience to significant deformation to prevent or even mitigate progressive collapse.

8. The results of this study encourage the use of RC structures constructed using special concrete because RuC can be utilized as an eco-friendly construction material to improve the ductility of RC elements and also provide an environmentally friendly solution to the disposal of waste tires.

The authors believe that additional concerted studies should be carried out in order to find new techniques to improve existing RC structures. Accordingly, the performance against progressive collapse would be enhanced. The fire resistance of RuC should also be investigated. Investigation of the effect of varying the degree of softness of crumb rubber on the mechanical characteristics of RuC mixtures is also warranted.

Author Contributions: Conceptualization, I.M.H.A., A.A.A. and K.S.; methodology, I.M.H.A. and A.A.A.; software and validation, I.M.H.A., M.A. and M.L.N.; writing—original draft preparation, I.M.H.A., R.T. and A.A.A.; writing—review and editing, M.A., R.T., M.L.N. and K.S.; funding acquisition, A.A.A. All authors have read and agreed to the published version of the manuscript.

Funding: This research was funded by Researchers Supporting Project number (RSP-2021/343), King Saud University, Riyadh, Saudi Arabia.

Institutional Review Board Statement: Not applicable.

Informed Consent Statement: Not applicable.

Data Availability Statement: Not applicable.

Conflicts of Interest: The authors declare no conflict of interest.

References

1. ASCE. *Minimum Design Loads and Associated Criteria for Buildings and Other Structures*; ASCE: Reston, VA, USA, 2017.
2. Bažant, Z.P.; Zhou, Y.J. Why did the world trade center collapse?—Simple analysis. *J. Eng. Mech.* **2002**, *128*, 2–6.
3. Pearson, C.; Delatte, N.J. Ronan point apartment tower collapse and its effect on building codes. *J. Perform. Constr. Facil.* **2005**, *19*, 172. [CrossRef]
4. Osteraas, J.D. Murrah building bombing revisited: A qualitative assessment of blast damage and collapse patterns. *J. Perform. Constr. Facil.* **2006**, *20*, 330–335. [CrossRef]
5. Lu, X.; Guan, H.; Sun, H.; Li, Y.; Zheng, Z.; Fei, Y.; Yang, Z.; Zuo, L. A preliminary analysis and discussion of the condominium building collapse in surfside, Florida, US, June 24, 2021. *Front. Struct. Civ.* **2021**, *15*, 1097–1110. [CrossRef]
6. Liu, X.-Y.; Qin, W.-H.; Xu, Z.-D.; Xi, Z.; Zhang, Z.-C. Investigation on the progressive collapse resistance of three-dimensional concrete frame structures reinforced by steel-FRP composite bar. *J. Build. Eng.* **2022**, *59*, 105116. [CrossRef]
7. British Standard Institute (BIS). *Structural Use of Concrete, Part 1: Code of Practice for Design and Construction*; British Standard Institute: London, UK, 1997.
8. European Committee for Standardization (CEN). *Eurocode 1: Actions on Structures. Part 1–7: General Actions-Accidental Actions*; European Committee for Standardization: Brussels, Belgium, 2006.
9. GSA. *Progressive Collapse Analysis and Design Guidelines for New Federal Office Buildings and Major Modernization Projects*; GSA: Washington, DC, USA, 2003.
10. Department of Defense (DoD). *Design of Buildings to Resist Progressive Collapse: Unified Facilities Criteria (UFC) 4-023-03*; Department of Defense: Washington, DC, USA, 2010.
11. *CECS 392-2014*; Code for Anti-Collapse Design of Building Structures. China Association for Engineering Construction Standardization (CECS): Bejing, China, 2014.
12. Alogla, K.; Weekes, L.; Augusthus-Nelson, L. A new mitigation scheme to resist progressive collapse of RC structures. *Constr. Build. Mater.* **2016**, *125*, 533–545. [CrossRef]
13. Li, Z.; Liu, Y.; Huo, J.; Rong, H.; Chen, J.; Elghazouli, A.Y. Experimental assessment of fire-exposed RC beam-column connections with varying reinforcement development lengths subjected to column removal. *Fire Saf. J.* **2018**, *99*, 38–48. [CrossRef]
14. Lu, X.; Lin, K.; Gu, D.; Li, Y. Experimental Study of Novel Concrete Frames Considering Earthquake and Progressive Collapse. In *Concrete Structures in Earthquake*; Springer: Berlin/Heidelberg, Germany, 2019; pp. 29–45.
15. Qian, K.; Li, B. Strengthening of multibay reinforced concrete flat slabs to mitigate progressive collapse. *J. Struct. Eng.* **2015**, *141*, 04014154. [CrossRef]
16. Liu, T.; Xiao, Y.; Yang, J.; Chen, B. CFRP Strip Cable Retrofit of RC Frame for Collapse Resistance. *J. Compos. Constr.* **2016**, *21*, 04016067. [CrossRef]

17. Ali, B.H.; Mete Güneyisi, E.; Bigonah, M. Assessment of Different Retrofitting Methods on Structural Performance of RC Buildings against Progressive Collapse. *Appl. Sci.* **2022**, *12*, 1045. [CrossRef]
18. Elsayed, W.M.; Moaty, M.A.A.; Issa, M.E. Effect of reinforcing steel debonding on RC frame performance in resisting progressive collapse. *HBRC J.* **2016**, *12*, 242–254. [CrossRef]
19. Hrabova, K.; Teply, B.; Vymazal, T. Sustainability assessment of concrete mixes. In Proceedings of the IOP Conference Series: Earth and Environmental Science, Changsha, China, 18–20 September 2020; p. 012021.
20. Lehner, P.; Horňáková, M. Effect of Amount of Fibre and Damage Level on Service Life of SFR Recycled Concrete in Aggressive Environment. *Buildings* **2021**, *11*, 489. [CrossRef]
21. Ismail, M.K.; Hassan, A.A. Ductility and cracking behavior of reinforced self-consolidating rubberized concrete beams. *J. Mater. Civ. Eng.* **2017**, *29*, 04016174. [CrossRef]
22. Mendis, A.S.; Al-Deen, S.; Ashraf, M.J.C.; Materials, B. Flexural shear behaviour of reinforced Crumbed Rubber Concrete beam. *Constr. Build. Mater.* **2018**, *166*, 779–791. [CrossRef]
23. Zheng, L.; Huo, X.S.; Yuan, Y.J. Strength, modulus of elasticity, and brittleness index of rubberized concrete. *J. Mater. Civ. Eng.* **2008**, *20*, 692–699. [CrossRef]
24. Sadek, D.M.; El-Attar, M.M. Structural behavior of rubberized masonry walls. *J. Clean. Prod.* **2015**, *89*, 174–186. [CrossRef]
25. Ahmed, D.A.; Jumaa, G.B.; Khalighi, M.J.C.; Materials, B. Mechanical properties and shear strength of rubberized fibrous reinforced concrete beams without stirrups. *Constr. Build. Mater.* **2022**, *350*, 128796. [CrossRef]
26. Noaman, A.T.; Bakar, B.A.; Akil, H.M.; Alani, A. Fracture characteristics of plain and steel fibre reinforced rubberized concrete. *Constr. Build. Mater.* **2017**, *152*, 414–423. [CrossRef]
27. Son, K.S.; Hajirasouliha, I.; Pilakoutas, K. Strength and deformability of waste tyre rubber-filled reinforced concrete columns. *Constr. Build. Mater.* **2011**, *25*, 218–226. [CrossRef]
28. Ganesan, N.; Raj, B.; Shashikala, A. Behavior of self-consolidating rubberized concrete beam-column joints. *ACI Mater. J.* **2013**, *110*, 697.
29. Huang, X.; Ranade, R.; Ni, W.; Li, V.C. On the use of recycled tire rubber to develop low E-modulus ECC for durable concrete repairs. *Constr. Build. Mater.* **2013**, *46*, 134–141. [CrossRef]
30. Issa, C.A.; Salem, G. Utilization of recycled crumb rubber as fine aggregates in concrete mix design. *Constr. Build. Mater.* **2013**, *42*, 48–52. [CrossRef]
31. Guo, Y.-C.; Zhang, J.-H.; Chen, G.-M.; Xie, Z.-H. Compressive behaviour of concrete structures incorporating recycled concrete aggregates, rubber crumb and reinforced with steel fibre, subjected to elevated temperatures. *J. Clean. Prod.* **2014**, *72*, 193–203. [CrossRef]
32. Alwesabi, E.A.; Abu Bakar, B.S.; Alshaikh, I.M.H.; Akil, H.M. Experimental investigation on mechanical properties of plain and rubberised concretes with steel–polypropylene hybrid fibre. *Constr. Build. Mater.* **2020**, *233*, 117194. [CrossRef]
33. Yu, J.; Tan, K.H. Structural behavior of RC beam-column subassemblages under a middle column removal scenario. *J. Struct. Eng.* **2013**, *139*, 233–250. [CrossRef]
34. Ahmadi, R.; Rashidian, O.; Abbasnia, R.; Mohajeri Nav, F.; Usefi, N. Experimental and numerical evaluation of progressive collapse behavior in scaled RC beam-column subassemblage. *Shock Vib.* **2016**, *2016*, 3748435. [CrossRef]
35. Almusallam, T.; Al-Salloum, Y.; Ngo, T.; Mendis, P.; Abbas, H. Experimental investigation of progressive collapse potential of ordinary and special moment-resisting reinforced concrete frames. *Mater. Struct.* **2017**, *50*, 137. [CrossRef]
36. Elsanadedy, H.M.; Almusallam, T.H.; Al-Salloum, Y.A.; Abbas, H. Investigation of precast RC beam-column assemblies under column-loss scenario. *Constr. Build. Mater.* **2017**, *142*, 552–571. [CrossRef]
37. Lim, N.S.; Tan, K.; Lee, C. Effects of rotational capacity and horizontal restraint on development of catenary action in 2-D RC frames. *Eng. Struct.* **2017**, *153*, 613–627. [CrossRef]
38. Gu, X.-L.; Zhang, B.; Wang, Y.; Wang, X.-L. Experimental investigation and numerical simulation on progressive collapse resistance of RC frame structures considering beam flange effects. *J. Build. Eng.* **2021**, *42*, 102797. [CrossRef]
39. Kang, S.-B.; Wang, S.; Gao, S. Analytical study on one-way reinforced concrete beam-slab sub-structures under compressive arch action and catenary action. *Eng. Struct.* **2020**, *206*, 110032. [CrossRef]
40. Qian, K.; Li, B. Performance of three-dimensional reinforced concrete beam-column substructures under loss of a corner column scenario. *J. Struct. Eng.* **2013**, *139*, 584–594. [CrossRef]
41. Qian, K.; Li, B.J.A.S.J. Slab effects on response of reinforced concrete substructures after loss of corner column. *ACI Struct. J.* **2012**, *109*, 845–855.
42. Qian, K.; Li, B.J.A.S.J. Resilience of flat slab structures in different phases of progressive collapse. *ACI Struct. J.* **2016**, *113*, 537–548. [CrossRef]
43. Ibrahim AL-Shaikh, N.F. Numerical Analysis of Masonry-Infilled Reinforced Concrete Frames. *J. Sci. Technol.* **2014**, *19*, 21–28.
44. Altheeb, A.; Alshaikh, I.M.; Abadel, A.; Nehdi, M.; Alghamdi, H.J. Effects of Non-Structural Walls on Mitigating the Risk of Progressive Collapse of RC Structures. *Lat. Am. J. Solids Struct.* **2022**, *19*, e440. [CrossRef]
45. Alshaikh, I.M.; Bakar, B.A.; Alwesabi, E.A.; Akil, H.M. Experimental investigation of the progressive collapse of reinforced concrete structures: An overview. *Structures* **2020**, *25*, 881–900. [CrossRef]
46. Kiakojouri, F.; De Biagi, V.; Chiaia, B.; Sheidaii, M.R. Progressive collapse of framed building structures: Current knowledge and future prospects. *Eng. Struct.* **2020**, *206*, 110061. [CrossRef]

47. Alshaikh, I.M.; Bakar, B.A.; Alwesabi, E.A.; Akil, H.M. Progressive collapse of reinforced rubberised concrete: Experimental study. *Constr. Build. Mater.* **2019**, *226*, 307–316. [CrossRef]
48. Deng, X.-F.; Liang, S.-L.; Fu, F.; Qian, K. Effects of high-strength concrete on progressive collapse resistance of reinforced concrete frame. *J. Struct. Eng.* **2020**, *146*, 04020078. [CrossRef]
49. Alshaikh, I.M.; Bakar, B.A.; Alwesabi, E.A.; Zeyad, A.M.; Magbool, H.M. Finite element analysis and experimental validation of progressive collapse of reinforced rubberized concrete frame. *Structures* **2021**, *33*, 2361–2373. [CrossRef]
50. Alshaikh, I.M.; Bakar, B.A.; Alwesabi, E.A.; Abadel, A.A.; Alghamdi, H.; Altheeb, A.; Tuladhar, R.J. Progressive collapse behavior of steel fiber-reinforced rubberized concrete frames. *J. Build. Eng.* **2022**, *57*, 104920. [CrossRef]
51. Ismail, M.K.; Hassan, A.A.A. Shear behaviour of large-scale rubberized concrete beams reinforced with steel fibres. *Constr. Build. Mater.* **2017**, *140*, 43–57. [CrossRef]
52. ACI. *Building Code Requirements for Structural Concrete and Commentary*; American Concrete Institute: Indianapolis, IN, USA, 2011.
53. ETABS-CSI. *Integrated Finite Element Analysis and Design of Structures Basic Analysis Reference Manual, 17*; Computers and Structures Inc: Berkeley, CA, USA, 2018.
54. ABAQUS. *User Assistance*; Dassault Systèmes Simulia Corporation: Providence, RI, USA, 2019.
55. Lubliner, J.; Oliver, J.; Oller, S.; Oñate, E. A plastic-damage model for concrete. *Int. J. Solids Struct.* **1989**, *25*, 299–326. [CrossRef]
56. Lee, J.; Fenves, G.L. Plastic-damage model for cyclic loading of concrete structures. *J. Eng. Mech.* **1998**, *124*, 892–900. [CrossRef]
57. Hognestad, E. *Study of Combined Bending and Axial Load in Reinforced Concrete Members*; University of Illinois at Urbana Champaign, College of Engineering: Champaign, IL, USA, 1951.
58. Stoner, J. *Finite Element Modelling of GFRP Reinforced Concrete Beams*; University of Waterloo: Waterloo, ON, Canada, 2015.
59. Wang, T.; Hsu, T.T. Nonlinear finite element analysis of concrete structures using new constitutive models. *Comput. Struct.* **2001**, *79*, 2781–2791. [CrossRef]
60. Bi, K.; Ren, W.-X.; Cheng, P.-F.; Hao, H. Domino-type progressive collapse analysis of a multi-span simply-supported bridge: A case study. *Eng. Struct.* **2015**, *90*, 172–182. [CrossRef]
61. Botez, M.; Bredean, L.; Ioani, A. Improving the accuracy of progressive collapse risk assessment: Efficiency and contribution of supplementary progressive collapse resisting mechanisms. *Comput. Struct.* **2016**, *174*, 54–65. [CrossRef]
62. Nguyen, V.-Q.; Nizamani, Z.A.; Park, D.; Kwon, O.-S. Numerical simulation of damage evolution of Daikai station during the 1995 Kobe earthquake. *Eng. Struct.* **2020**, *206*, 110180. [CrossRef]
63. Pham, A.T.; Tan, K.H.; Yu, J. Numerical investigations on static and dynamic responses of reinforced concrete sub-assemblages under progressive collapse. *Eng. Struct.* **2017**, *149*, 2–20. [CrossRef]
64. Shi, Y.; Li, Z.-X.; Hao, H. A new method for progressive collapse analysis of RC frames under blast loading. *Eng. Struct.* **2010**, *32*, 1691–1703. [CrossRef]
65. Wu, K.-C.; Li, B.; Tsai, K.-C. The effects of explosive mass ratio on residual compressive capacity of contact blast damaged composite columns. *J. Constr. Steel Res.* **2011**, *67*, 602–612. [CrossRef]
66. Luccioni, B.M.; Aráoz, G.F.; Labanda, N.A. Defining erosion limit for concrete. *Int. J. Prot. Struct.* **2013**, *4*, 315–340. [CrossRef]
67. Tang, E.K.; Hao, H. Numerical simulation of a cable-stayed bridge response to blast loads, Part I: Model development and response calculations. *Eng. Struct.* **2010**, *32*, 3180–3192. [CrossRef]
68. Kumar, V.; Kartik, K.; Iqbal, M. Experimental and numerical investigation of reinforced concrete slabs under blast loading. *Eng. Struct.* **2020**, *206*, 110125. [CrossRef]
69. Titoum, M.; Tehami, M.; Achour, B.; Jaspart, J.-P. Analysis of semi-continuous composite beams with partial shear connection using 2-D finite element approach. *Asian J. Appl. Sci.* **2008**, *1*, 185–205. [CrossRef]
70. *A615/A615M-03a*; Specification for Deformed and Plain Carbon-Steel Bars for Concrete Reinforcement. ASTM International: Conshohocken, PA, USA, 2003.
71. Hradil, P.; Talja, A. Ductility Limits of High Strength Steels; Online at FIMECC Research Portal and VTT. 2016. Available online: https://cris.vtt.fi/en/publications/ductility-limits-of-high-strength-steels (accessed on 15 September 2022).
72. Bridgman, P.W. *Studies in Large Plastic Flow and Fracture*; Harvard University Press: Cambridge, MA, USA, 1964.
73. Baltay, P.; Gjelsvik, A. Coefficient of friction for steel on concrete at high normal stress. *J. Mater. Civ. Eng.* **1990**, *2*, 46–49. [CrossRef]
74. Dat, P.X.; Tan, K.H. Experimental response of beam-slab substructures subject to penultimate-external column removal. *J. Struct. Eng.* **2015**, *141*, 04014170. [CrossRef]
75. Eren, N.; Brunesi, E.; Nascimbene, R. Influence of masonry infills on the progressive collapse resistance of reinforced concrete framed buildings. *Eng. Struct.* **2019**, *178*, 375–394. [CrossRef]
76. Pham, A.T.; Lim, N.S.; Tan, K.H. Investigations of tensile membrane action in beam-slab systems under progressive collapse subject to different loading configurations and boundary conditions. *Eng. Struct.* **2017**, *150*, 520–536. [CrossRef]
77. Huang, H.; Huang, M.; Zhang, W.; Guo, M.; Liu, B. Progressive collapse of multistory 3D reinforced concrete frame structures after the loss of an edge column. *Struct. Infrastruct. Eng.* **2022**, *18*, 249–265. [CrossRef]
78. Lu, X.; Lin, K.; Li, Y.; Guan, H.; Ren, P.; Zhou, Y. Experimental investigation of RC beam-slab substructures against progressive collapse subject to an edge-column-removal scenario. *Eng. Struct.* **2017**, *149*, 91–103. [CrossRef]
79. Qian, K.; Li, B.; Ma, J.-X. Load-carrying mechanism to resist progressive collapse of RC buildings. *J. Struct. Eng.* **2015**, *141*, 04014107. [CrossRef]

80. Ren, P.; Li, Y.; Lu, X.; Guan, H.; Zhou, Y. Experimental investigation of progressive collapse resistance of one-way reinforced concrete beam–slab substructures under a middle-column-removal scenario. *Eng. Struct.* **2016**, *118*, 28–40. [CrossRef]
81. Masi, A.; Digrisolo, A.; Santarsiero, G. Analysis of a Large Database of Concrete Core Tests with Emphasis on Within-Structure Variability. *Materials* **2019**, *12*, 1985. [CrossRef]
82. Alwesabi, E.A.; Bakar, B.A.; Alshaikh, I.M.; Akil, H.M. Impact resistance of plain and rubberized concrete containing steel and polypropylene hybrid fiber. *Mater. Today Commun.* **2020**, *25*, 101640. [CrossRef]
83. Alwesabi, E.A.; Bakar, B.A.; Alshaikh, I.M.; Zeyad, A.M.; Altheeb, A.; Alghamdi, H. Experimental investigation on fracture characteristics of plain and rubberized concrete containing hybrid steel-polypropylene fiber. *Structures* **2021**, *33*, 4421–4432. [CrossRef]